Lewis Acid Enhancement of Proton Induced CO_2 Cleavage: Bond Weakening and Ligand Residence Time Effects

Joshua A. Buss, David G. VanderVelde, and Theodor Agapie*

Division of Chemistry and Chemical Engineering, California Institute of Technology, 1200 East California Boulevard, MC 127-72, Pasadena, California 91125, United States

Supporting Information

Contents

Experimental Details
General Considerations S3
Modified Synthesis of **1** S3
Synthesis of **2** S4
Synthesis of **3** S4
Synthesis of **4** S5
Synthesis of **P2Mo(CO)** S5
Synthesis of **6** S6

NMR Spectra
Figure S1—^{1}H NMR Spectrum of **1** S7
Figure S2—^{31}P{^{1}H} NMR Spectrum of **1** S7
Figure S3—^{1}H NMR Spectrum of **2** S7
Figure S4—^{13}C{^{1}H} NMR Spectrum of **2** S8
Figure S5—^{31}P{^{1}H} NMR Spectrum of **2** S8
Figure S6—^{1}H NMR Spectrum of **3** S8
Figure S7—^{31}P{^{1}H} NMR Spectrum of **3** S9
Figure S8—^{11}B{^{1}H} NMR Spectrum of **3** S9
Figure S9—^{19}F NMR Spectrum of **3** S9
Figure S10—^{1}H NMR Spectrum of **4** S10
Figure S11—^{13}C{^{1}H} NMR Spectrum of **4** S10
Figure S12—^{31}P{^{1}H} NMR Spectrum of **4** S10
Figure S13—^{19}F NMR Spectrum of **4** S11
Figure S14—^{1}H NMR Spectrum of **P2Mo(CO)** S11
Figure S15—^{13}C{^{1}H} NMR Spectrum of **P2Mo(CO)** S11
Figure S16—^{31}P{^{1}H} NMR Spectrum of **P2Mo(CO)** S12
Figure S17—^{1}H NMR Spectrum of **6** S12
Figure S18—^{13}C{^{1}H} NMR Spectrum of **6** S12
Figure S19—^{31}P{^{1}H} NMR Spectrum of **6** S13

IR Spectra
Figure S20—Fourier Transform Infrared Spectra of **2/2-$^{13}CO_2$** S14
Figure S21—Fourier Transform Infrared Spectra of **1** and **3** S14
Figure S22—Fourier Transform Infrared Spectra of **4/4-$^{13}CO_2$** S15
Figure S23—Fourier Transform Infrared Spectra of **P2Mo($^{12/13}$CO)** S15
Figure S24—Fourier Transform Infrared Spectra of **2/2-$^{13}CO_2$** + $B(C_6H_2F_3)_3$ S16

*In Situ Preparation of Lewis Acid Adducts of **2-^{13}C***
Representative Procedure for Lewis Acid AN Determination S17
Table S1—Lewis Acid Acceptor Number Determination S17
Representative Procedure for in situ Lewis Acid Adduct Generation S17
Figure S25—Stacked Partial $^{13}C\{^1H\}$ NMR Spectra of *in situ* Generated Lewis Acid Adducts of **2-^{13}C** in 2 PhCl : Et_2O S18
Figure S26—Stacked Partial $^{13}C\{^1H\}$ NMR Spectra of *in situ* Generated Lewis Acid Adducts of **2-^{13}C** in PhCl S18
Figure S27—Stacked Partial $^{31}P\{^1H\}$ NMR Spectra of *in situ* Generated Lewis Acid Adducts of **2-^{13}C**
Table S2—NMR Data for Lewis Acid Adducts of **3** S19

Small Molecule Exchange Measurements
Figure S28—T_1 Measurements for an Equilibrium Mixture of **1-^{15}N/2-^{13}C** S20
Table S3—Inversion Recovery D for and Equilibrium Mixture of **1-^{15}N/2-^{13}C** S20
Figure S29—Equilibrium Constant Determination for a Mixture of **1-^{15}N/2-^{13}C** S21
Figure S30—PRESAT $^{13}C\{^1H\}$ NMR spectrum (126 MHz, C_6D_6, 25 °C) demonstrating saturation transfer from free CO_2 (124.8 ppm) to bound CO_2 (191.9 ppm). S21
General Procedure for Isotope Exchange Kinetics S22
Table S4—CO_2 Exchange Rate as a Function of LA Identity S23
Figure S31—Representative $^{12/13}CO_2$ Exchange Data in 2 PhCl : Et_2O S23
Figure S32—Representative $^{12/13}CO_2$ Exchange Data in PhCl S24
Table S5—Linearized CO_2 Exchange Rate as a Function of LA Identity S24
Figure S33—Linearized $^{12/13}CO_2$ Exchange Data in 2 PhCl : Et_2O S25
Figure S34—Linearized $^{12/13}CO_2$ Exchange Data in PhCl S25

CO_2 Protonation Reactions
Scheme S1—Proposed Mechanism for C–O Bond Cleavage S26
Table S6—C–O Bond Cleavage as a Function of LA Additive S27
Table S7—Comparison of CO_2 Activation, Kinetic Stabilization, and Protonation Data S28
Figure S35—Graphical Comparison of C–O Cleavage, Residence Time, and CO_2-adduct Chemical Shift S28
Figure S36—^{19}F NMR Spectra Tracking Speciation of $B(C_6F_5)_3$ During Protonation S29

Crystallographic Information
Refinement Details S30
Table S8—Crystal and Refinement Data for Complexes **2-4**, **6**, **7**, and **P2Mo(CO)** S31
Figure S37—Structural Drawing of **2** S32
Figure S38—Structural Drawing of **3** S32
Figure S39—Structural Drawing of **4** S33
Figure S40—Structural Drawing of **6** S33
Figure S41—Structural Drawing of **7** S34

References S35

General Considerations

Unless otherwise specified, all operations were carried out in an MBraun drybox under a nitrogen atmosphere or using standard Schlenk and vacuum line techniques. Solvents for air- and moisture-sensitive reactions were dried over sodium benzophenone ketyl, calcium hydride, or by the method of Grubbs.[1] Deuterated solvents were purchased from Cambridge Isotope Laboratories and vacuum transferred from sodium benzophenone ketyl (C_6D_6) or CaH_2 (CD_3CN). Solvents, once dried and degassed, were vacuum transferred directly prior to use or stored under inert atmosphere over activated 4 Å molecular sieves. **[P2Mo(CO)$_2$][2OTf]**,[2] potassium graphite (KC_8),[3] $CsBAr^F{}_{24}$,[3] $NaBAr^F{}_{24}$,[4] $B(C_6H_2F_3)_3$,[5] $B(C_6F_5)_3$,[6] $B(C_6H_3(CF_3)_2)_3$,[7] and Brookhart's acid ($[H(Et_2O)_2][BAr^F{}_{24}]$),[8] were prepared according to literature procedures. Commercial reagents were purchased from standard vendors and used without further purification unless noted otherwise. ^{1}H, ^{13}C{^{1}H}, and ^{31}P{^{1}H} NMR spectra were recorded on a Varian 400 MHz or Varian INOVA-500 MHz spectrometers with shifts reported in parts per million (ppm). ^{1}H and ^{13}C{^{1}H} NMR spectra are referenced to residual solvent peaks.[9] ^{31}P{^{1}H} chemical shifts are referenced to an external 85% H_3PO_4 (0 ppm) standard. Fourier transform infrared ATR spectra were collected from thin films or powders on a Thermo Scientific Nicolet iS5 Spectrometer with a diamond ATR crystal (utilized iD5 ATR insert).

*Modified Synthesis of **1***

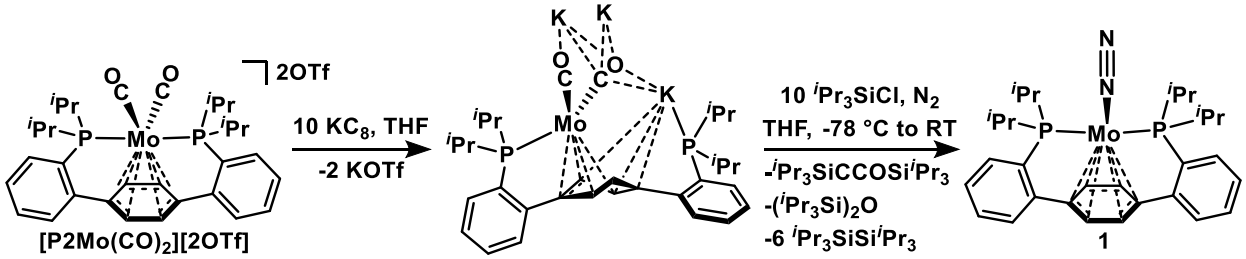

A 500 mL Teflon stoppered Schlenk tube was charged with [P2Mo(CO)$_2$][2OTf] (10.0 g, 10.96 mmol), KC_8 (14.8 g, 109.47 mmol), and a large stir bar. THF (100 mL) was added slowly with swirling, resulting in the formation of a dark purple slurry (Note: this process is quite exothermic and THF condensing on the walls of the flask is normal). Stirring was initiated and additional THF (300 mL) was added, giving a dark purple mixture. With a heavy N_2 counterflow, the Teflon stopper of the flask was exchanged with a septum. The flask was then cooled to -78 °C in a dry ice/acetone bath and ^{i}Pr$_3$SiCl (23.5 mL, 109.82 mmol) was added dropwise via syringe. Following this addition, the flask was re-stoppered and sealed. It was left to warm to room temperature, with stirring, during which time the color of the solution changed from deep purple to burgundy. The volatiles were removed *in vacuo*, providing a dark black/brown residue.

Hexanes (500 mL) was added via cannula and the flask contents shaken vigorously, giving a suspension of graphite in a dark red/brown solution. This mixture was subjected to filtration through a thick pad of celite. The reaction residue and the filter cake were extracted with hexanes until the washes were near colorless (*ca.* 1 L of solvent on this scale, 1.5 L of hexanes in total) and the combined filtrate was concentrated under reduced pressure to a volume of *ca.* 70 mL, precipitating microcrystals of **1**. These microcrystals were collected on a medium porosity fritted funnel, washed with cold (-78 °C) hexanes (*ca.* 20 mL), and dried *in vacuo*. The resulting red solids were collected as analytically pure **1** (4.1 g, 6.99 mmol, 64 % yield).

The spectroscopic data for **1** prepared in this way match prior literature.[2] Additionally, ^{1}H and ^{31}P{^{1}H} NMR of the described solids are presented in Figures S1 and S2, respectively.

*Synthesis of **2***

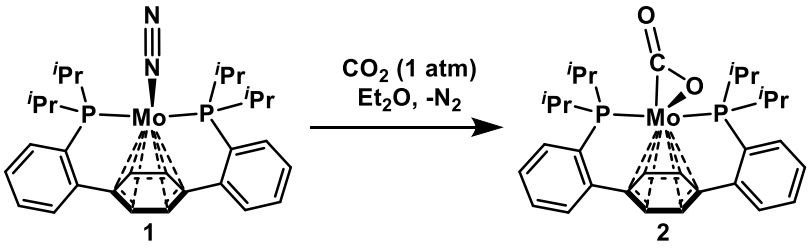

A 100 mL round bottom flask was charged with **1** (1.15 g, 1.96 mmol) and a stir bar. The flask was attached to a swivel frit apparatus and connected to a high vacuum line. Et_2O (70 mL) was admitted via vacuum transfer at -78 °C and stirring was initiated. The flask was allowed to warm to room temperature, providing a red orange homogeneous solution. A partial atmosphere of CO_2 (*ca.* 600 Torr) was admitted to the flask. After stirring for 30 sec., flocculent light orange solids precipitated from solution. Stirring continued for 5 min. The reaction vessel was partially degassed and the CO_2 atmosphere (*ca.* 600 Torr) was refreshed. This process was repeated thrice, with 5 min intervals of stirring in between each atmosphere exchange. The apparatus was subjected to vacuum and the total volume concentrated to *ca.* 40 mL. The suspension was filtered and the solids were washed twice via condensation of the filtrate solvent. All volatiles were removed *in vacuo*, giving **2** as an analytically pure pale orange powder (1.10 g, 1.82 mmol, 93%). Complex **2** is stable under a N_2 atmosphere in the solid state, but reverts to **1** in solution in the presence of N_2. ^{1}H NMR (400 MHz, C_6D_6, 23 °C) δ: 7.36 (d, *J* = 6.8 Hz, 2H, aryl-*H*), 7.11 (d, *J* = 5.2 Hz, 2H, aryl-H), 7.03 (t, *J* = 7.39 Hz, 2H, aryl-*H*), 6.97 (t, *J* = 6.10 Hz, 2H, aryl-*H*), 4.98 (s, 2H, central arene-*H*), 3.54-3.56 (m, 2H, central arene-*H*), 2.85-2.92 (m, 2H, C*H*$(CH_3)_2$), 2.45-2.57 (m, 2H, C*H*$(CH_3)_2$), 1.70-1.76 (m, 6H, CH(C*H*$_3)_2$), 1.04-1.10 (m, 6H, CH(C*H*$_3)_2$), 0.92-0.96 (m, 6H, CH(C*H*$_3)_2$), 0.57-0.63 (m, 6H, CH(C*H*$_3)_2$). ^{31}P{^{1}H} NMR (162 MHz, C_6D_6, 23 °C) δ: 62.67 (br s). IR (powder ATR, cm^{-1}): 1716, 1198.

2-^{13}C can be prepared analogously using $^{13}CO_2$ in lieu of CO_2. The enhanced ^{13}C{^{1}H} NMR (101 MHz, C_6D_6, 23 °C) resonance is observed at 191.89 (t, *J* = 29.9 Hz) ppm. The IR bands redshift to 1672 and 1177 cm^{-1}.

*Synthesis of **3***

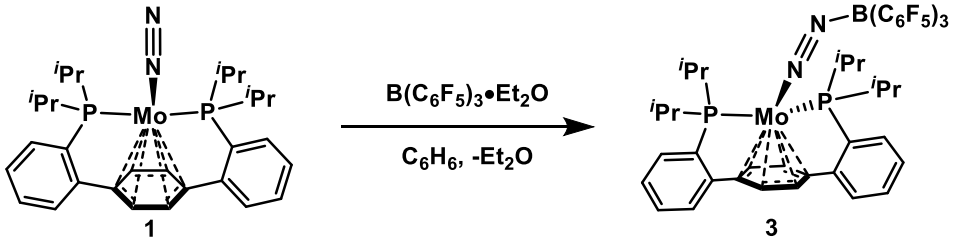

A 100 mL RB flask was charged with **1** (300 mg, 0.511 mmol), $B(C_6F_5)_3$•Et_2O (300 mg, 0.511 mmol), and a stir bar. PhMe (25 mL) was added, resulting in dissolution of the reagents and formation of a dark red/brown homogeneous solution. Stirring continued to 15 min. At this time, solvent was removed *in vacuo*, giving a dark residue. This residue was triturated with hexanes (4 mL) and dried under reduced pressure, affording crude **3**. Prepared this way, samples of **3** contain *ca.* 20% of an unidentified asymmetric impurity and 7% free diphosphine ligand. This mixture of products can be crystallized from cold PhMe (-35 °C), but NMR spectra of the crystals show both **3** and the impurity. Mechanical separation of the crystals under a microscope (in an effort to obtain a solids state structure of the impurity) proved unsuccessful. Further attempts to obtain pure **3** have thus far been unsuccessful. ^{1}H NMR (400 MHz, C_6D_6, 23 °C) δ: 7.22 (d, *J* = 7.32 Hz, 2H, aryl-*H*), 6.92-7.04 (m, 6H, aryl-*H*), 4.62 (s, 2H, central arene-*H*), 3.99 (s, 2H, central arene-*H*), 2.23-2.32 (m, 2H, C*H*$(CH_3)_2$), 2.00-2.09 (m, 2H, C*H*$(CH_3)_2$), 0.90-0.95 (m, 6H, CH(C*H*$_3)_2$), 0.75-0.85 (m, 18H, CH(C*H*$_3)_2$). ^{31}P{^{1}H} NMR (162 MHz, C_6D_6, 23 °C) δ: 68.71 (s). ^{11}B{^{1}H} NMR (128 MHz, C_6D_6, 23 °C) δ: -14.47 (s). ^{19}F NMR (376 MHz, C_6D_6, 23 °C) δ: -131.53 (br s), -158.24 (v br s), -164.51 (br s).

*Synthesis of **4***

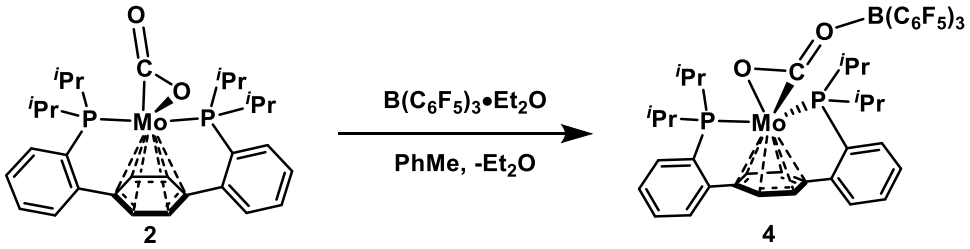

2 4

A 100 mL Teflon stoppered Schlenk tube was charged with **2** (300 mg, 0.498 mmol), $B(C_6F_5)_3$•Et_2O (291 mg, 0.498 mmol) and a stir bar. The flask was attached to a high vacuum line and evacuated. Toluene (25 mL) was condensed into the reaction vessel at -78 °C, and stirring was initiated. While warming to room temperature, orange **2** dissolved to give a deep red homogenous solution. The volume was reduced to *ca.* 5 mL under reduced pressure and transferred, in a glovebox, to a 20 mL scintillation vial. Upon standing for 12 hours at -35 °C, the precipitated maroon solids were collected on a medium porosity fritted funnel. Washing with cold hexanes (2 x 2 mL) afforded analytically pure **3** as the persisting solid material (462 mg, 0.415 mmol, 83 %). Complex **4** is stable in the presence of N_2 both in solution and as a solid, but is reactive toward coordinating solvents such as THF or MeCN. ^{1}H (500 MHz, C_6D_6, 25 °C) δ: 7.19 (s, 2H, aryl-*H*), 7.01 (t, *J* = 7.08 Hz, 2H, aryl-*H*), 6.94 (t, *J* = 7.44 Hz, 2H, aryl-*H*), 6.85-6.87 (m, 2H, aryl-*H*), 5.36 (br d, *J* = 2.34 Hz, 2H, central arene-*H*), 3.94 (s, 2H, central arene-*H*), 1.93-2.00 (m, 2H, C*H*$(CH_3)_2$), 1.78-1.86 (m, 2H, C*H*$(CH_3)_2$), 0.85-0.90 (m, 6H, CH(C*H*$_3)_2$), 0.78-0.81 (m, 6H, CH(C*H*$_3)_2$), 0.63-0.67 (m, 6H, CH(C*H*$_3)_2$), 0.38-0.43 (m, 6H, CH(C*H*$_3)_2$). ^{13}C{^{1}H} (126 MHz, C_6D_6, 25 °C) δ: 218.94 (t, *J* = 11.47 Hz, Mo-*C*O_2), 148.93 (app dt, *J* = 241.92 & 8.68 Hz, B(*C*$_6$F$_5)_3$), 146.47 (m, aryl-*C*), 146.27 (m, aryl-*C*), 140.08 (app dt, *J* = 248.72 & 14.84 Hz, B(*C*$_6$F$_5)_3$), 137.48 (ddd, *J* = 246.57, 19.91, & 9.95 Hz, B(*C*$_6$F$_5)_3$), 132.25 (s, aryl-*C*), 130.09 (s, aryl-*C*), 127.80 (s, aryl-*C*; coincides with residual C_6D_6 but corroborated by HMBC), 127.46 (s, aryl-*C*; coincides with residual C_6D_6 but corroborated by HMBC), 104.21 (t, *J* = 3.81 Hz, central arene-*C*), 85.40 (s, central arene-*C*), 82.66 (s, central arene-*C*), 27.87 (br d, *J* = 7.32 Hz, *C*H$(CH_3)_2$), 24.40 (br d, *J* = 7.30 Hz, *C*H$(CH_3)_2$), 20.72 (m, CH(*C*H$_3)_2$), 19.54 (s, CH(*C*H$_3)_2$), 18.01 (m, CH(*C*H$_3)_2$), 17.81 (m, CH(*C*H$_3)_2$). ^{31}P{^{1}H} (202 MHz, C_6D_6, 25 °C) δ: 50.47 (s, *P*$_2$). ^{19}F (470 MHz, C_6D_6, 25 °C) δ: -131.13 (d, *J* = 19.36 Hz, B(C$_6$*F*$_5)_3$), -159.58 (t, *J* = 20.87 Hz, B(C$_6$*F*$_5)_3$), -165.24 (m, B(C$_6$*F*$_5)_3$). IR (solid ATR, cm^{-1}): 1602, 1218.

4-^{13}C can be prepared analogously starting from **2-^{13}C**. The enhanced resonance in the ^{13}C NMR spectrum is the triplet at 219.94 ppm. No ^{2}*J*(P,C) scalar coupling is resolved in the ^{31}P{^{1}H} NMR spectrum. The IR bands (solid ATR) shift to 1565 and 1200 cm^{-1}.

Synthesis of **P2Mo(CO)**

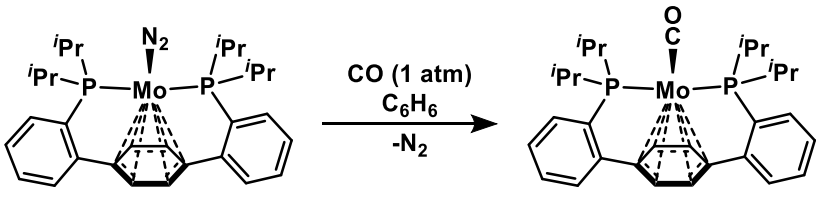

1 P2Mo(CO)

A Teflon stoppered Schlenk tube was charged with **5** (200 mg, 0.340 mmol), C_6H_6 (10 mL), and a stir bar. The resulting red solution was degassed thoroughly via three freeze-pump-thaw cycles. Following the final thaw, CO (1 atm) was admitted to the headspace of the flask. The stopper was sealed and the reaction left to stir for 1 hr. At this time, the solvent was lyophilized, providing **P2Mo(CO)** as an orange powder (196 mg, 0.340 mmol, >99%). ^{1}H NMR (400 MHz, C_6D_6, 23 °C) δ: 7.39-7.41 (m, 2H, aryl-*H*), 7.16 (br m, 2H,

aryl-*H*), 7.00-7.04 (m, 4H, aryl-*H*), 4.60 (br s, 2H, central arene-*H*), 4.59 (br m, 2H, central arene-*H*), 2.40-2.49 (m, 2H, C*H*(CH_3)$_2$), 2.11-2.20 (m, 2H, C*H*(CH_3)$_2$), 1.35-1.41 (m, 6H, CH(C*H*$_3$)$_2$), 1.07-1.13 (m, 6H, CH(C*H*$_3$)$_2$), 0.97-1.05 (m, 12H, CH(C*H*$_3$)$_2$). $^{13}C\{^1H\}$ NMR (101 MHz, C_6D_6, 23 °C) δ: 242.58 (t, *J* = 15.19 Hz, *C*O), 152.32 (vt, *J* = 12.24 Hz, aryl-*C*), 152.02 (vt, *J* = 11.99 Hz, aryl-*C*), 130.18 (s, aryl-*C*), 128.59 (s, aryl-*C*), 126.70 (vt, *J* = 2.03 Hz, aryl-*C*), 97.92 (t, *J* = 2.60 Hz, central arene-*C*), 90.21 (s, central arene-*C*), 76.49 (t, *J* = 1.61 Hz, central arene-*C*), 30.53 (vt, *J* = 5.16 Hz, *C*H(CH_3)$_2$), 29.62 (m, *C*H(CH_3)$_2$), 21.17 (vt, *J* = 4.76 Hz, CH(*C*H$_3$)$_2$), 19.88 (vt, *J* = 4.25 Hz, CH(*C*H$_3$)$_2$), 19.50 (s, CH(*C*H$_3$)$_2$), 18.92 (s, CH(*C*H$_3$)$_2$). $^{31}P\{^1H\}$ NMR (162 MHz, C_6D_6, 23 °C) δ: 82.06 (s). IR (powder sample, diamond ATR, cm^{-1}) ν_{CO} = 1798.

P2Mo(¹³CO) was prepared analogously, using ^{13}CO in lieu of CO; the enhanced resonance in the $^{13}C\{^1H\}$ NMR spectrum is the triplet at 242.60 ppm. The $^{31}P\{^1H\}$ NMR signal at 82.06 ppm splits into a doublet (*J* = 15.91 Hz). IR (powder sample, diamond ATR, cm^{-1}) ν_{13CO} = 1758.

*Synthesis of **6***

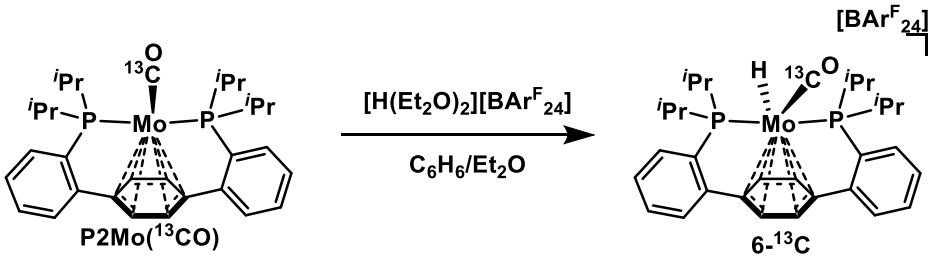

A 20 mL scintillation vial was charged with a deep orange solution of **P2Mo(¹³CO)** (200 mg, 0.340 mmol) in C_6H_6 (10 mL). With stirring, an ethereal solution of [H(Et_2O)$_2$][BAr^F_{24}] (345 mg, 0.340 mmol, in 5 mL) was added dropwise. The reaction mixture was dried *in vacuo* and the resulting residue triturated with hexanes (5 mL) and dried under reduced pressure, affording **6-¹³C** as a yellow/orange powder (468 mg, 0.323 mmol, 95 %). X-ray quality crystals were grown via vapor diffusion of pentane into an MeCN/Et_2O solution of **6-¹³C**. ^1H (500 MHz, CD_3CN, 25 °C) δ: 7.71 (br s, 8H, BAr^F_{24} *ortho-H*), 7.67 (br s, 4H, BAr^F_{24} *para-H*), 7.57-7.62 (m, 6H, aryl-*H*), 7.52-7.55 (m, 2H, aryl-*H*), 6.29 (br s, 2H, central arene-*H*), 5.92 (br d, *J* = 1.05 Hz, 2H, central arene-*H*), 2.82-2.93 (m, 2H, C*H*(CH_3)$_2$), 2.62-2.71 (m, 2H, C*H*(CH_3)$_2$), 1.28-1.32 (m, 6H, CH(C*H*$_3$)$_2$), 1.19-1.21 (m, 6H, CH(C*H*$_3$)$_2$), 1.16-1.18 (m, 6H, CH(C*H*$_3$)$_2$), 0.90-0.94 (m, 6H, CH(C*H*$_3$)$_2$), -3.02 (td, *J* = 65.37 & 4.02 Hz, 1H, Mo-*H*). $^{13}C\{^1H\}$ (126 MHz, CD_3CN, 25 °C) δ: 221.81 (t, *J* = 13.82 Hz, Mo-*C*O), 162.62 (q, *J* = 49.28 Hz, BAr^F_{24} aryl-*C*), 145.16 (d, *J* = 20.71 Hz, aryl-*C*), 142.82 (dd, *J* = 28.66 & 1.83 Hz, aryl-*C*), 135.67 (br d, *J* = 20.15 Hz, BAr^F_{24} aryl-*C*), 132.36 (vt, *J* = 8.55 Hz, aryl-*C*), 132.03 (vt, *J* = 7.36 Hz, aryl-*C*), 130.06 (m, aryl-*C*), 129.95 (qq, *J* = 32.02 & 2.83 Hz, BAr^F_{24} aryl-*C*), 128.15 (dvt, *J* = 11.93 & 9.54 Hz, aryl-*C*), 125.48 (q, *J* = 271.73 Hz, BAr^F_{24} *C*F_3), 118.93 (d, *J* = 4.24 Hz, central arene-*C*), 118.68 (br d, *J* = 15.72 Hz, BAr^F_{24} aryl-*C*), 98.86 (t, *J* = 2.03 Hz, central arene-*C*), 90.69 (s, central arene-*C*), 33.26 (d, *J* = 31.94 Hz, *C*H(CH_3)$_2$), 29.33 (d, *J* = 29.93 Hz, *C*H(CH_3)$_2$), 20.31 (d, *J* = 1.82 Hz, CH(*C*H$_3$)$_2$), 19.59 (d, *J* = 1.69 Hz, CH(*C*H$_3$)$_2$), 19.14 (d, *J* = 3.07 Hz, CH(*C*H$_3$)$_2$), 18.40 (s, CH(*C*H$_3$)$_2$).$^{31}P\{^1H\}$ (202 MHz, CD_3CN, 25 °C) δ: 93.01 (dd, *J* = 13.68 & 9.92 Hz, *P2*).

NMR Spectra

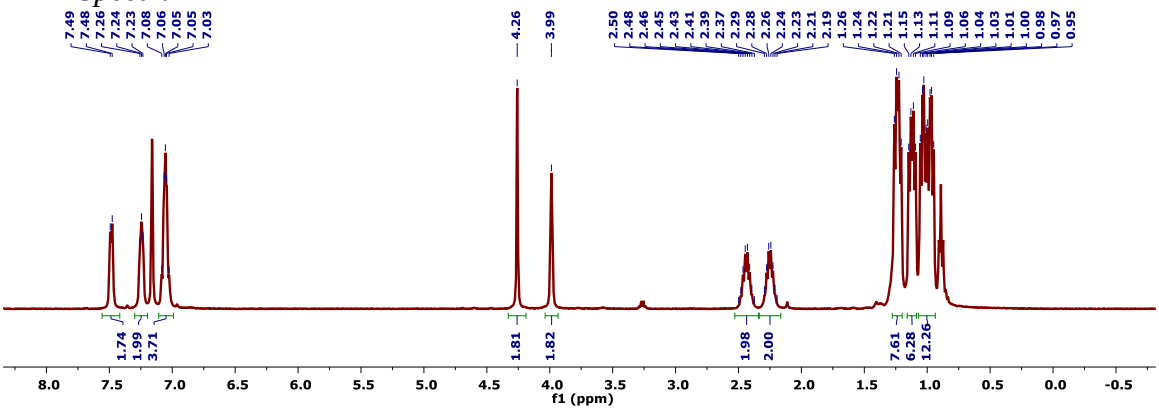

Figure S1—^{1}H NMR Spectrum (400 MHz, C_6D_6, 23°C) of as prepared **1**.

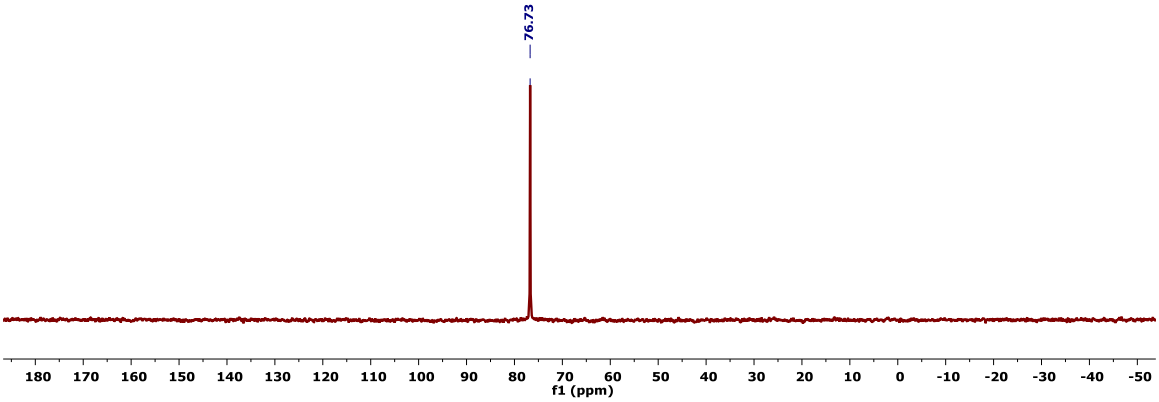

Figure S2—^{31}P{^{1}H} NMR Spectrum (162 MHz, C_6D_6, 23°C) of as prepared **1**.

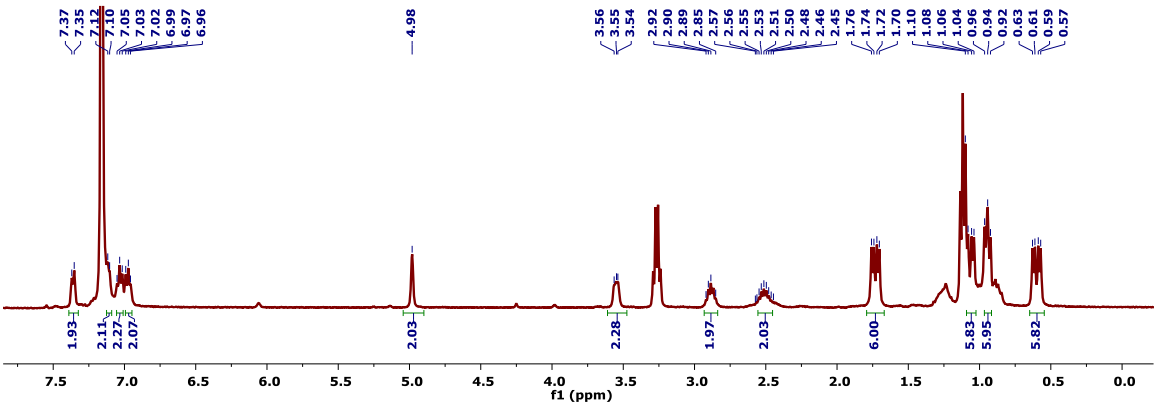

Figure S3—^{1}H NMR spectrum (400 MHz, C_6D_6, 23 °C) of **2**.

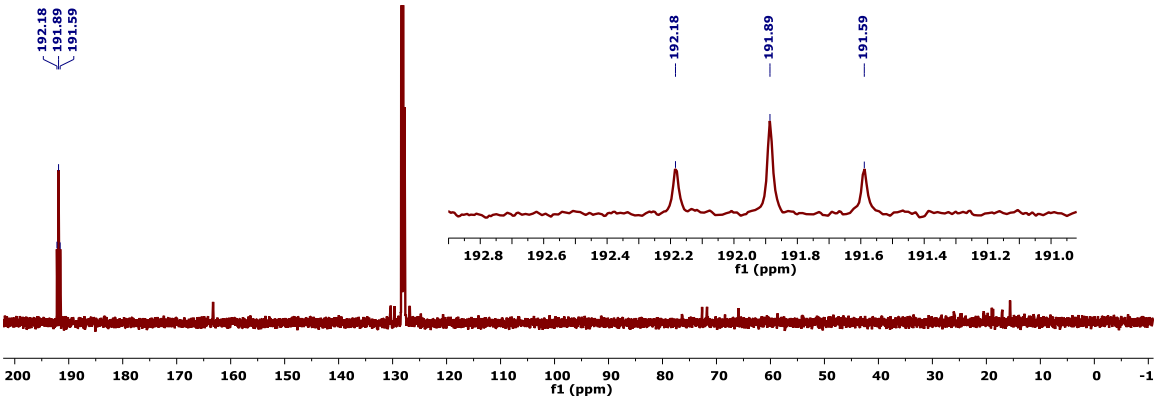

Figure S4—$^{13}C\{^{1}H\}$ NMR spectrum (101 MHz, C_6D_6, 23 °C) of **2-^{13}C**.

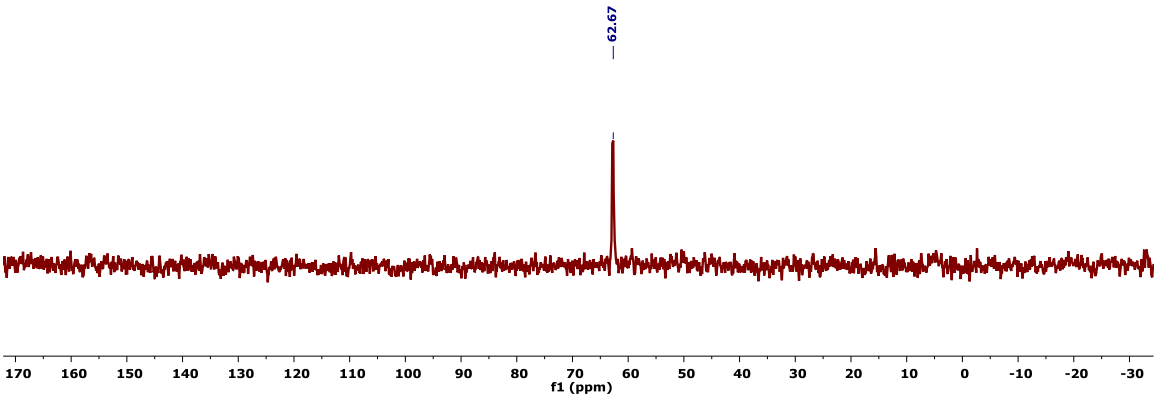

Figure S5—$^{31}P\{^{1}H\}$ NMR spectrum (162 MHz, C_6D_6, 23 °C) of **2**.

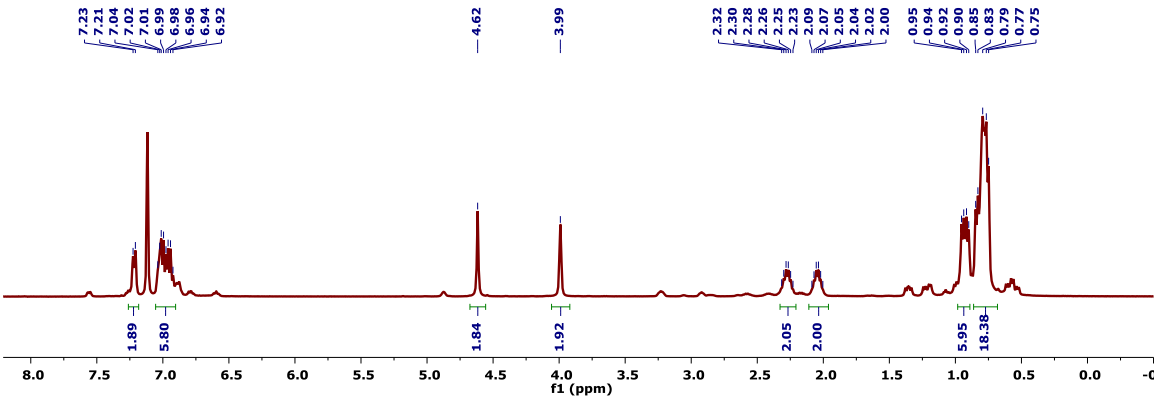

Figure S6—^{1}H NMR spectrum (400 MHz, C_6D_6, 23 °C) of a reaction mixture comprised primarily of **3.**

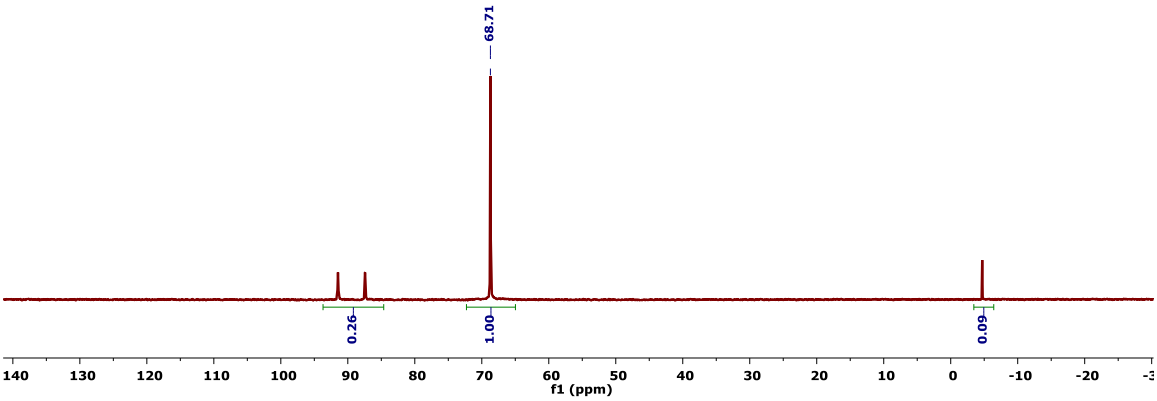

Figure S7—$^{31}P\{^{1}H\}$ NMR spectrum (162 MHz, C_6D_6, 23 °C) of a reaction mixture comprised primarily of **3.**

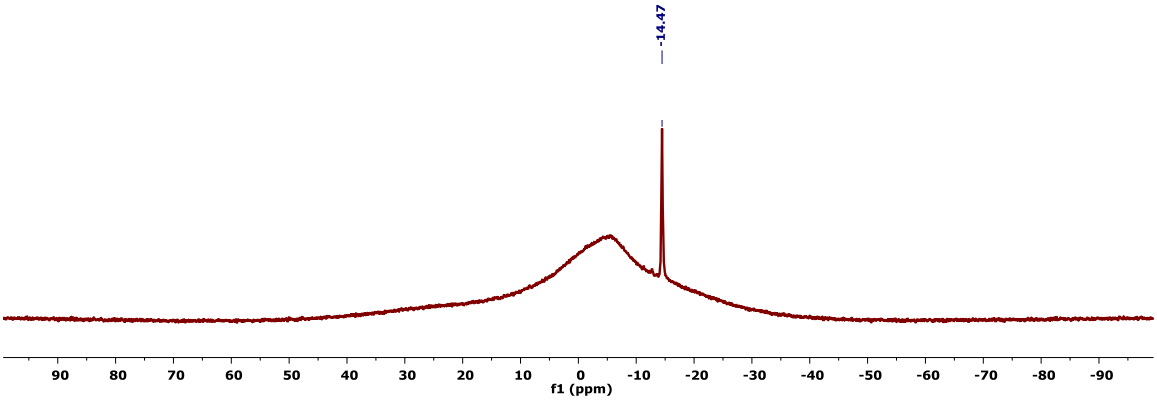

Figure S8—$^{11}B\{^{1}H\}$ NMR spectrum (128 MHz, C_6D_6, 23 °C) of a reaction mixture comprised primarily of **3.**

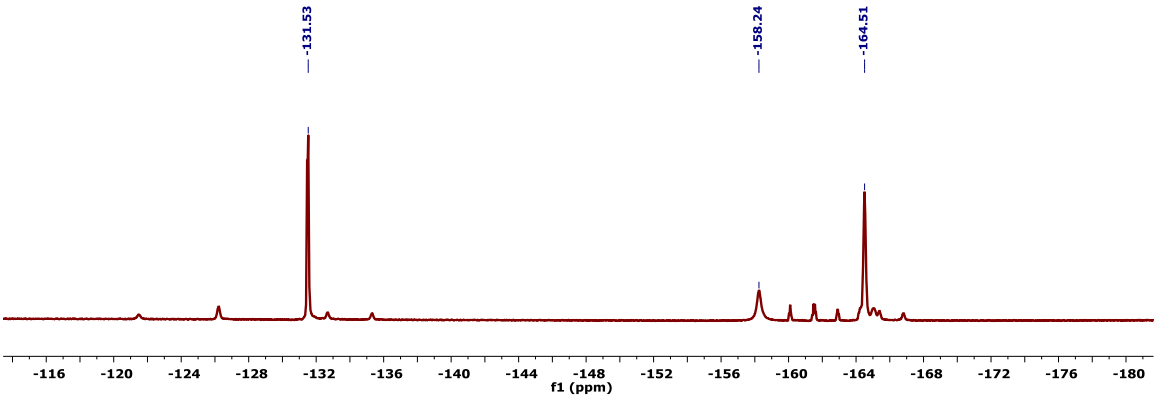

Figure S9—^{19}F NMR spectrum (376 MHz, C_6D_6, 23 °C) of a reaction mixture comprised primarily of **3.**

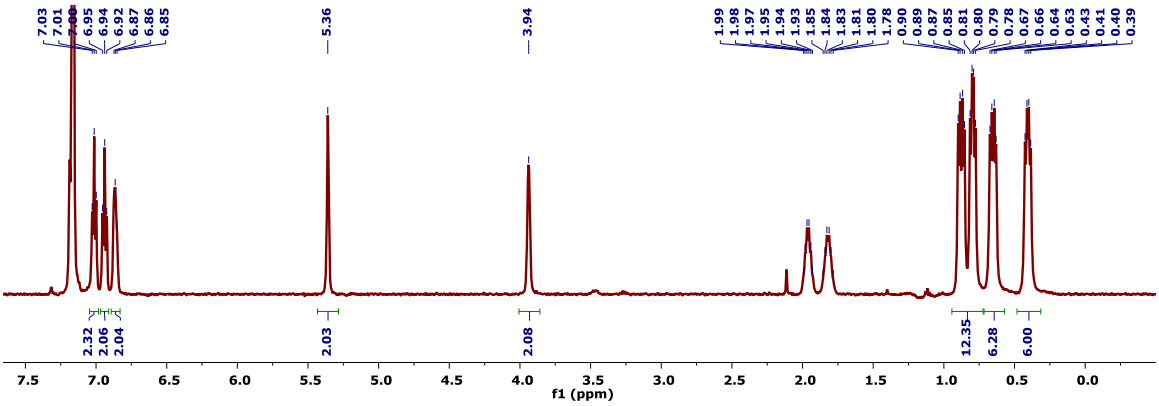

Figure S10—^{1}H NMR Spectrum (400 MHz, C_6D_6, 23°C) of **4**.

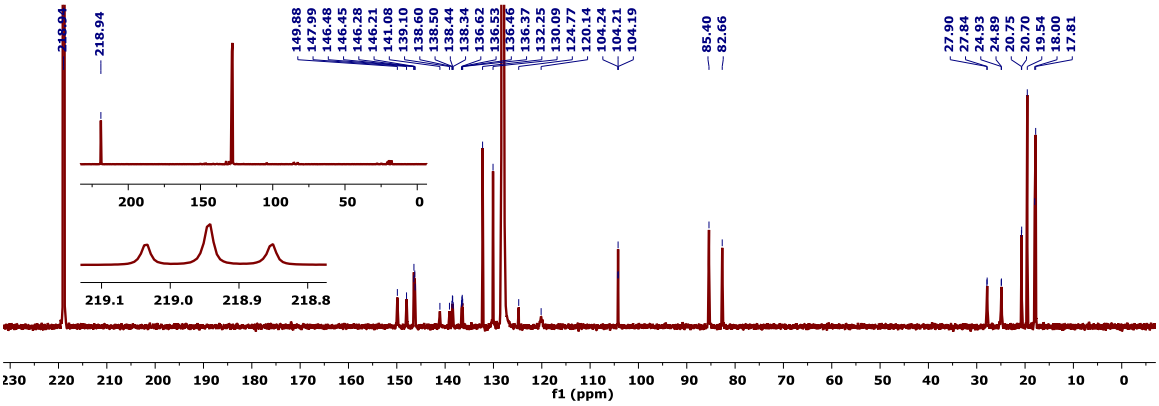

Figure S11—^{13}C{^{1}H} NMR Spectrum (101 MHz, C_6D_6, 23°C) of **4-^{13}C**. The insets show an untopped spectrum (top) and an enlargement of the $^{13}CO_2$ resonance (bottom).

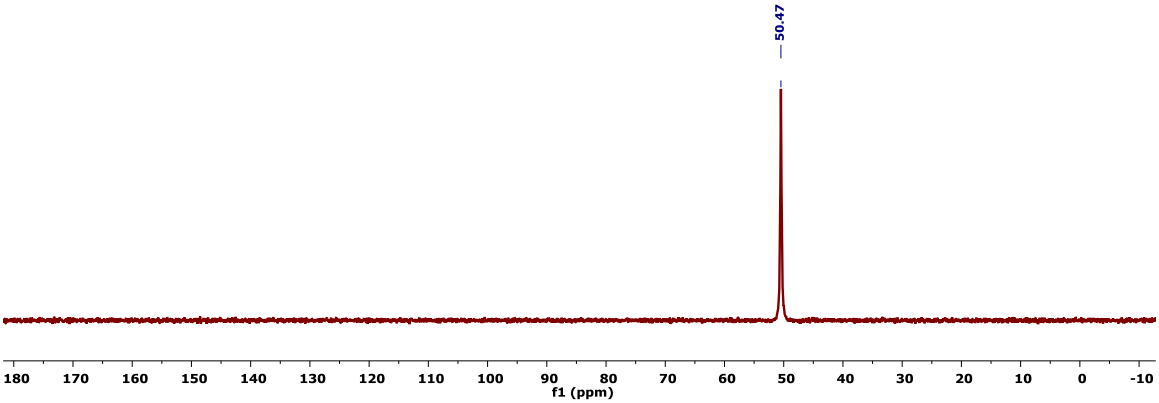

Figure S12—^{31}P{^{1}H} NMR Spectrum (162 MHz, C_6D_6, 23°C) of **4**.

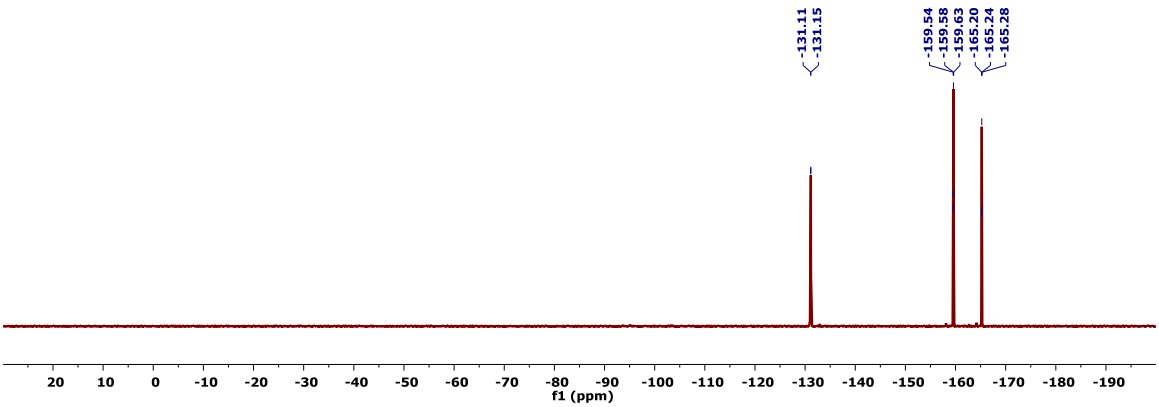

Figure S13—^{19}F NMR spectrum (376 MHz, C_6D_6, 23 °C) of **4**.

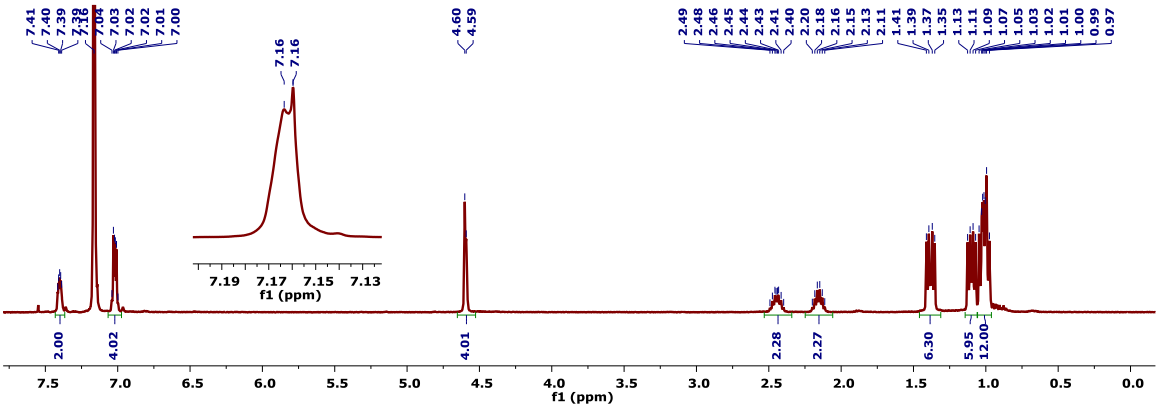

Figure S14—^{1}H NMR Spectrum (400 MHz, C_6D_6, 23 °C) of **P2Mo(CO)**. The inset shows a phenylene proton resonance that coincides with residual C_6D_5H at 7.16 ppm.

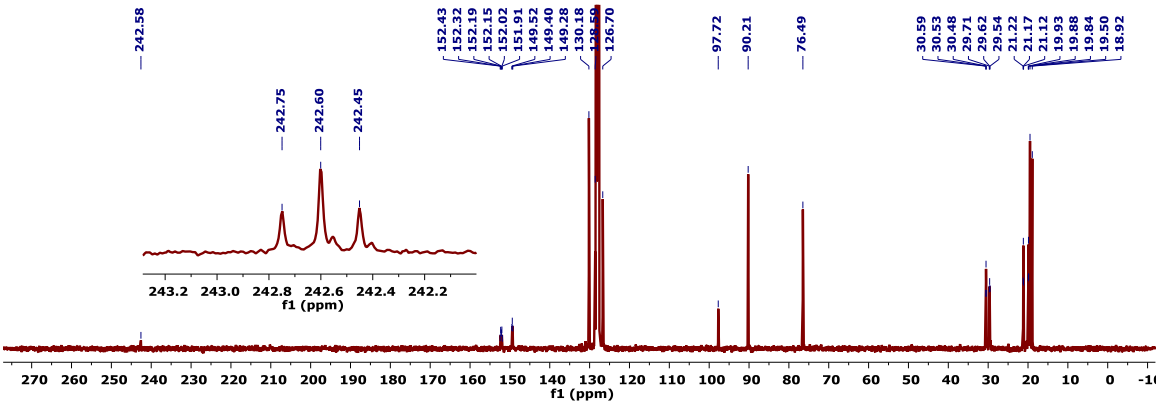

Figure S15—^{13}C{^{1}H} NMR Spectrum (101 MHz, C_6D_6, 25°C) of **P2Mo(CO)**. The inset shows the enhanced ^{13}C signals for **P2Mo(**^{13}**CO)**.

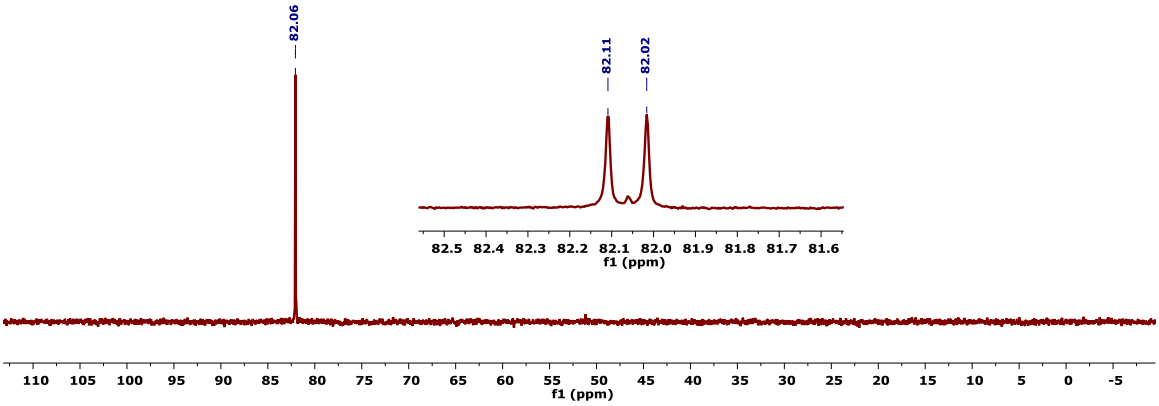

Figure S16—$^{31}P\{^{1}H\}$ NMR Spectrum (162 MHz, C_6D_6, 25°C) of **P2Mo(CO)**. The inset shows a partial $^{31}P\{^{1}H\}$ NMR spectrum for **P2Mo(**^{13}**CO)**.

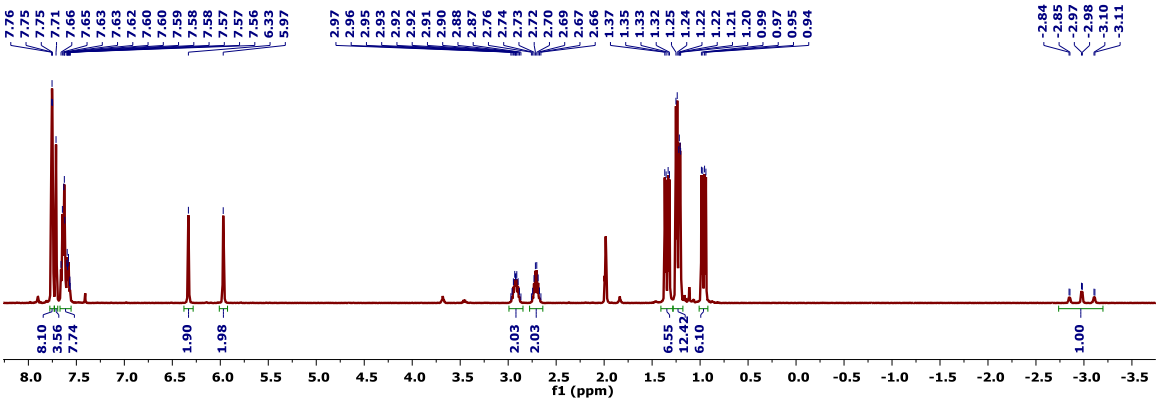

Figure S17—^{1}H NMR Spectrum (400 MHz, C_6D_6, 23°C) of **6-**^{13}**C**.

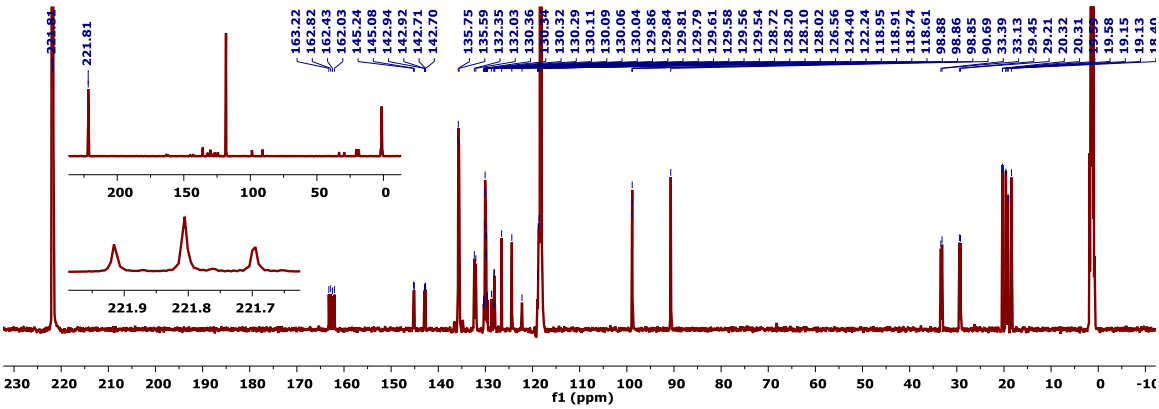

Figure S18—$^{13}C\{^{1}H\}$ NMR Spectrum (101 MHz, C_6D_6, 23°C) of **6-**^{13}**C**. The insets show an untopped spectrum (top) and an enlargement of the ^{13}CO resonance (bottom).

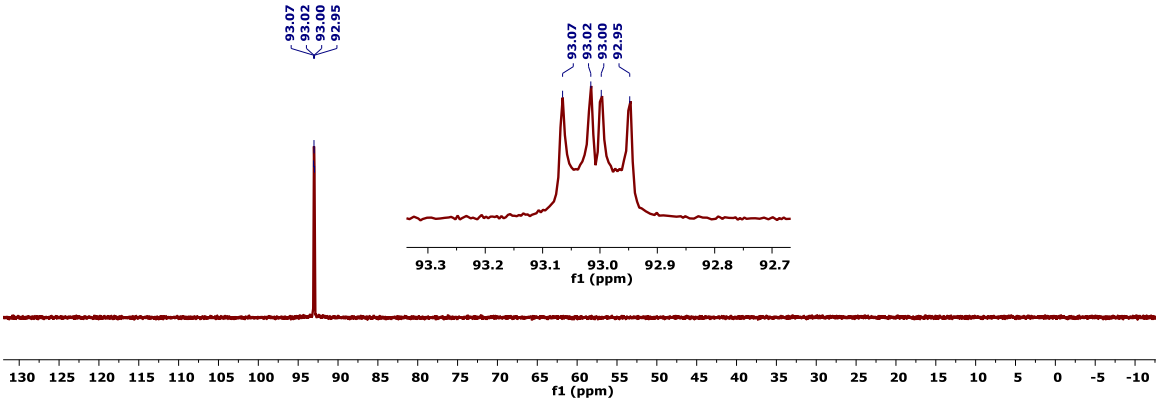

Figure S19—$^{31}P\{^{1}H\}$ NMR Spectrum (162 MHz, C_6D_6, 23°C) of **6-^{13}C**. The inset shows an enlargement of the relevant resonance, with well-defined ^{2}J(P,C) and ^{2}J(P,H) scalar coupling.

IR Spectra

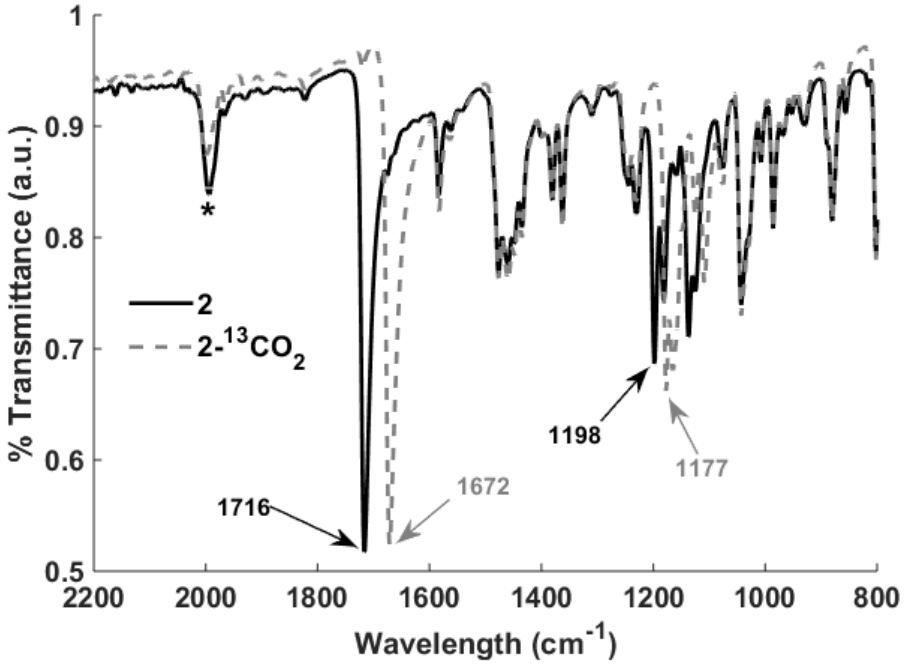

Figure S20—ATR IR Spectra of isotopologs **2**/**2-^{13}C**. The signals sensitive to CO_2 isotope enrichment are demarcated with arrows.

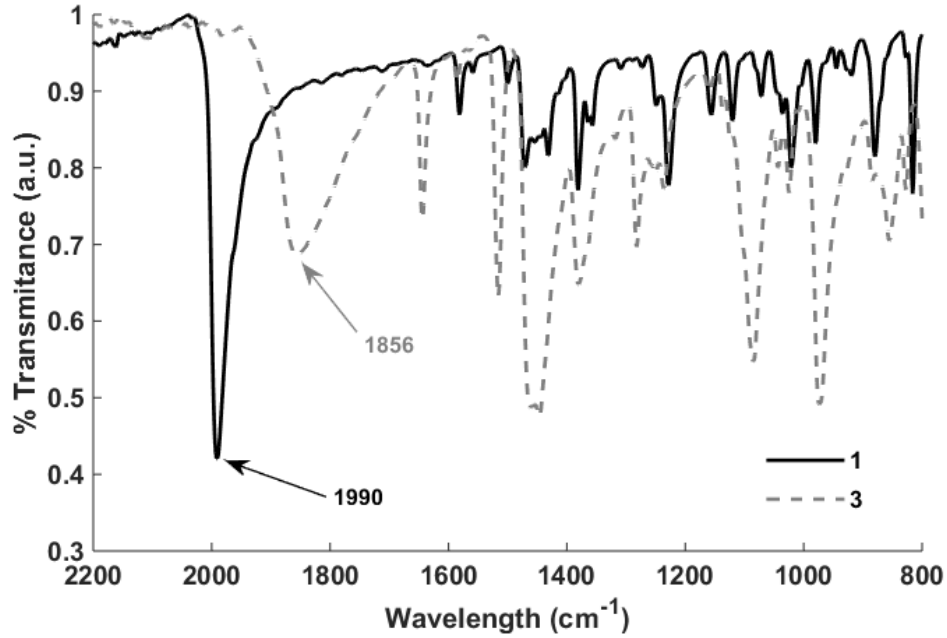

Figure S21—ATR IR Spectra of Mo(0) N_2 complex, **1**, and its $B(C_6F_5)_3$ adduct, **3**.

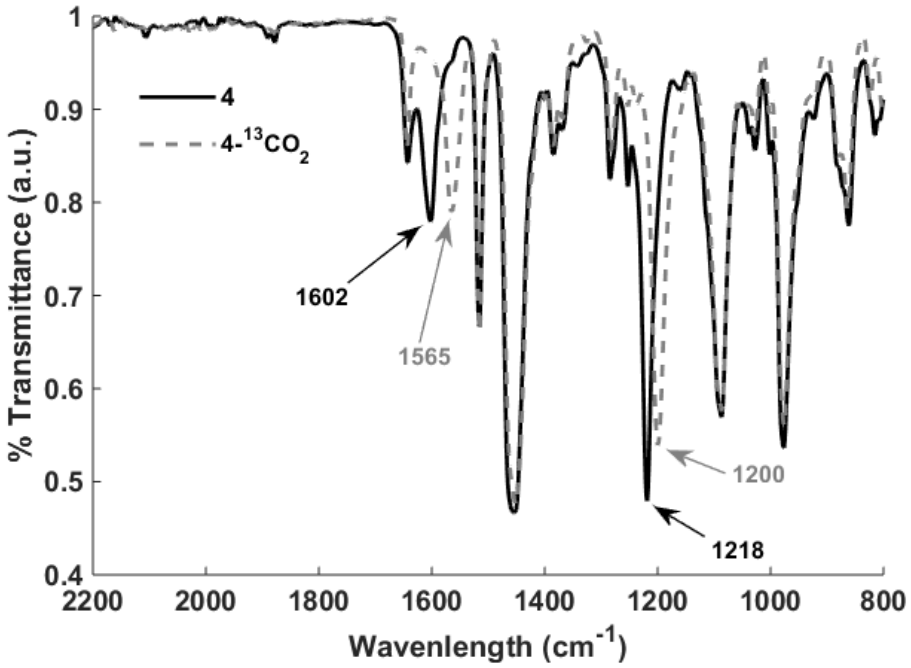

Figure S22—ATR IR Spectra of **4**/**4-^{13}C**. The signals sensitive to CO_2 isotope enrichment are demarcated with arrows.

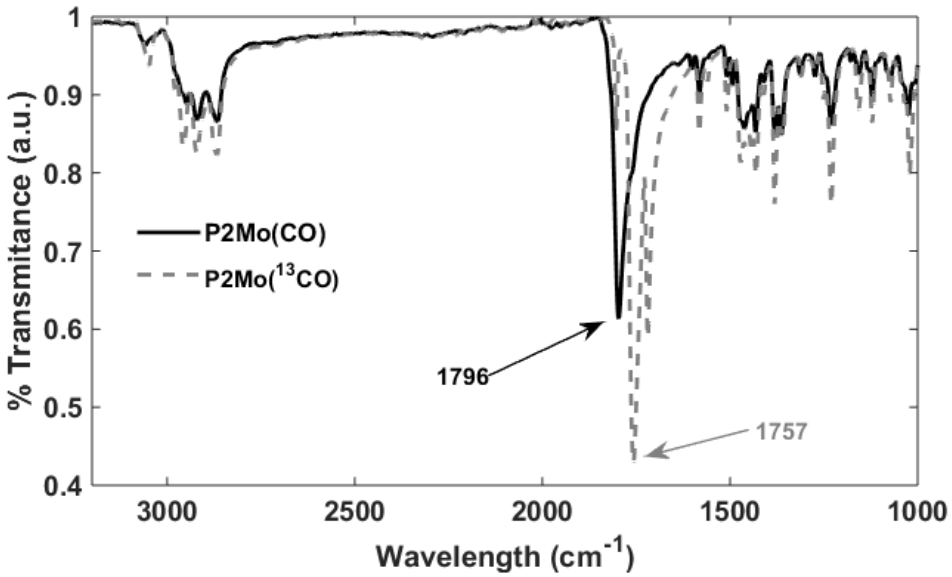

Figure S23—ATR IR Spectra of **P2Mo($^{12/13}$CO)**. The difference in the stretching frequency of the ^{12}C and ^{13}C isotopologs matches well with values calculated using a simple oscillator model and the respective reduced masses.

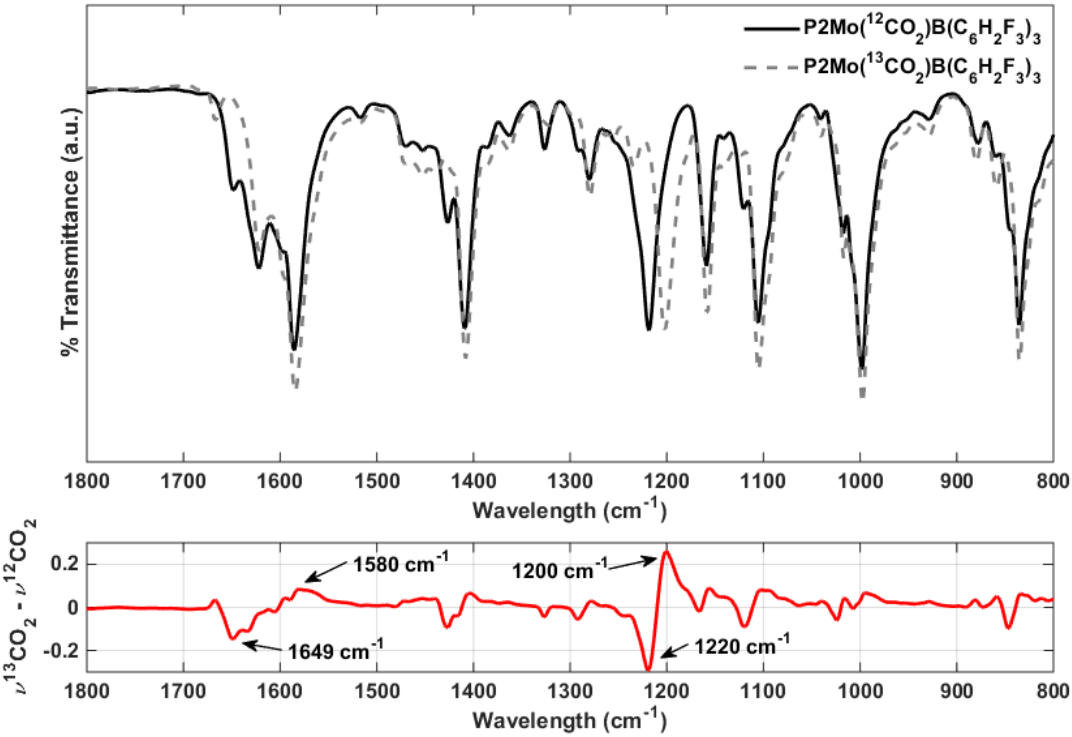

Figure S24—ATR IR Spectra of the product of reacting **2**(—) and **2-$^{13}CO_2$**(- -) with $B(C_6H_2F_3)_3$. The residual obtained from subtracting the ^{12}C isotopolog spectrum from that of the ^{13}C isotopolog is shown below, with the CO_2 relevant resonances labeled.

*In Situ Preparation of Lewis Acid Adducts of **3***

To ensure strict exclusion of N_2, solvents used for the preparation of LA adducts of **3** were thoroughly degassed via three freeze-pump-thaw cycles and vacuum transferred prior to use. The 2 PhCl : Et_2O stock solutions used for generation of LA adducts and kinetics experiments were prepared in 12 mL batches by sequentially vacuum transferring PhCl (8 mL) and Et_2O (4 mL) into a calibrated volume and then a storage flask sealed with a Teflon stopper. Solvents prepared this way were stored and manipulated under Ar.

Representative Procedure for LA AN Determination
In a N_2 filled glovebox, a J. Young NMR tube was charged with Et_3PO (4.5 mg, 0.033 mmol), 1,3,5-trimethoxybenzene (10 mg, 0.059 mmol), and LA (0.033 mmol). The tube was sealed and attached to a high vacuum line. Following thorough evacuation of the headspace, the J. Young tube was backfilled with Ar gas. Under a heavy Ar counterflow, solvent (0.5 mL) was added via syringe. The tube was sealed and the contents mixed, affording a colorless homogeneous solution. The tube was introduced to an NMR probe, pre-cooled to 0 °C. After allowing 10 min for temperature equilibration, $^{31}P\{^{1}H\}$ NMR spectra were collected.

The AN was calculated using the following equation:

$$AN = 2.21 \times (\delta\ ^{31}P - 41.0)$$

Table S1—Lewis Acid Acceptor Number Determination

Solvent	**2 PhCl : Et_2O**		**PhCl**	
LA	**δ ^{31}P (ppm)**	**AN**	**δ ^{31}P (ppm)**	**AN**
None	46.63	12.4	46.98	13.2
Cs(BAr^F_{24})	51.70	23.6	--	--
Na(BAr^F_{24})	55.39	31.8	--	--
Na(BAr^F_{24})	55.65	32.4	--	--
$B(C_6H_2F_3)_3$	71.82	68.1	71.70	67.8
$B(C_6F_5)_3$	76.82	79.2	76.34	78.1
$B(C_6H_3(CF_3)_2)_3$	--	--	78.43	82.7

Representative Procedure for LA Adduct Preparation
In a representative procedure, a J. Young NMR tube was charged with **2-^{13}C** (20 mg, 0.033 mmol), 1,3,5-trimethoxybenzene (10 mg, 0.059 mmol), and LA (0.033 mmol). The tube was sealed and attached to a high vacuum line. Following thorough evacuation of the headspace, the J. Young tube was backfilled with Ar gas. Under a heavy Ar counterflow, solvent (0.5 mL) was added via syringe. The tube was sealed and the contents mixed, affording a deep red homogeneous solution. Samples prepared this way were used for kinetics studies (*vide infra*) as well as adduct characterization.

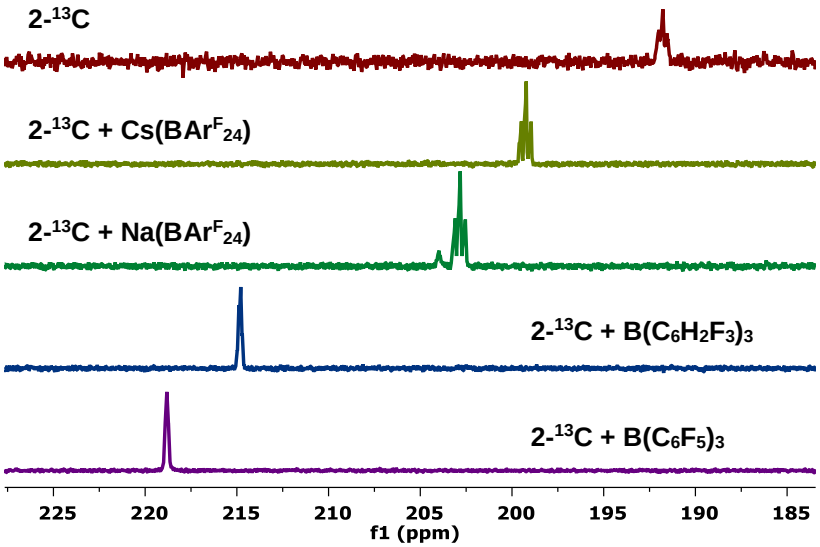

Figure S25—Stacked Partial $^{13}C\{^{1}H\}$ NMR Spectra (2 PhCl : Et_2O, 0°C,126 MHz) of *in situ* Generated Lewis Acid Adducts of **2-^{13}C**. The identity of the LA is indicated on each trace.

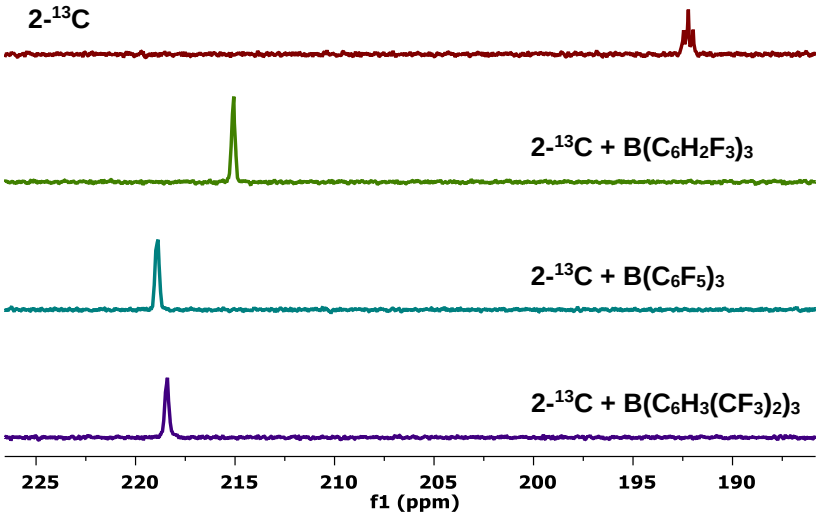

Figure S26—Stacked Partial $^{13}C\{^{1}H\}$ NMR Spectra (PhCl, 0°C,126 MHz) of *in situ* Generated Lewis Acid Adducts of **2-^{13}C**. The identity of the LA is indicated on each trace.

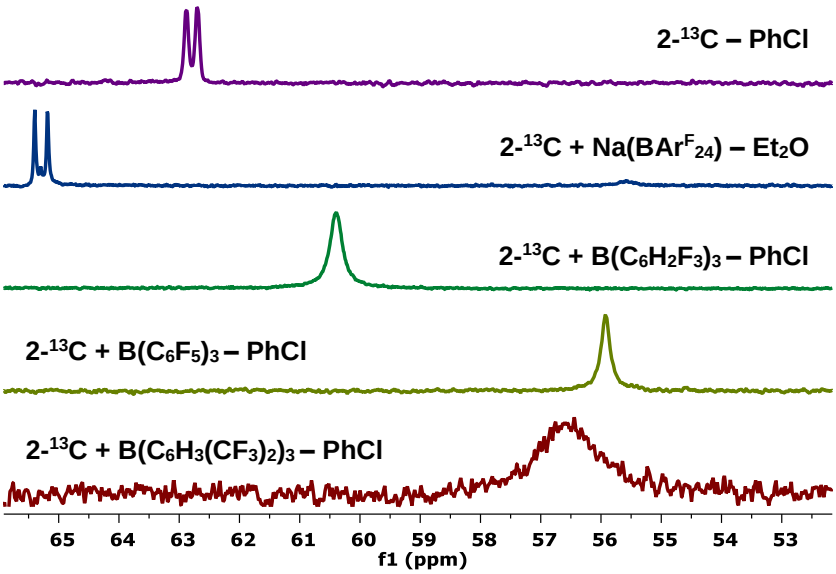

Figure S27—Stacked Partial $^{31}P\{^{1}H\}$ NMR Spectra of *in situ* Generated Lewis Acid Adducts of **2-^{13}C**. The identity of the LA and the solvent used are indicated on each trace.

Table S2—Compiled NMR Data for Lewis Acid Adducts of **3.**

LA	AN	δ $^{13}CO_2$ (ppm)	$^{2}J_{(P,C)}$ (Hz)	δ ^{31}P (ppm)
None	12.4	192.3	28.4	62.8
Cs(BAr$^{F}_{24}$)	23.6	199.9	34.0	--
Na(BAr$^{F}_{24}$)	31.8	203.5	34.1	65.3
B($C_6H_2F_3$)$_3$	68.1	215.7	8.21	60.4
B(C_6F_5)$_3$	79.2	219.6	NR‡	55.9
B($C_6H_3(CF_3)_2$)$_3$	82.7	219.1	10.0	56.6

‡The $^{2}J_{(P,C)}$ is not resolved in either the $^{31}P\{^{1}H\}$ or $^{13}C\{^{1}H\}$ NMR spectra.

Small Molecule Exchange Rate Measurements

To determine the equilibrium constant for the interconversion of **1** and **2**, a mixture was prepared as follows. A J. Young NMR tube was charged with a deep red C_6D_6 (0.6 mL) solution of **1** (20 mg, 0.034 mmol). The tube was sealed and attached to a high vacuum line. The contents of the tube were degassed via three freeze-pump-thaw cycles. $^{13}CO_2$ (*ca.* 500 Torr) was admitted to the tube, which was subsequently sealed a mixed. The solution lightened slightly, and an orange precipitate formed. The tube was submerged in LN_2 and the N_2 liberated upon $^{13}CO_2$ binding was removed *in vacuo*. This process was repeated twice more, thawing and mixing the reaction between degassing. ^{1}H and $^{31}P\{^{1}H\}$ NMR spectroscopy evidenced complete conversion of **1** to **2-^{13}C**. The tube was carefully opened to vacuum, removing any free $^{13}CO_2$, as confirmed by $^{13}C\{^{1}H\}$ NMR spectroscopy. Finally, the tube was submerged in LN_2, the headspace evacuated, and $^{15}N_2$ (*ca.* 300 Torr) was admitted to the tube. The J. Young tube was sealed, removed from the LN_2, and carefully thawed. A mixture of **1-^{15}N** and **2-^{13}C** was observed by $^{31}P\{^{1}H\}$ NMR spectroscopy. After 12 h, the same ratio of **1-^{15}N** to **2-^{13}C** was observed, suggesting equilibrium had been reached.

To obtain accurate integral values for the relative concentrations of **1-^{15}N**, free $^{15}N_2$, **2-^{13}C**, and free $^{13}CO_2$, T_1 scalar relaxation times were measured for representative resonances of each species (Figure S28 and Table S3). ^{15}N and $^{13}C\{^{1}H\}$ spectra were then collected with d_1 times of 25 s and 100 s, respectively (5 x T_1). The equilibrium constant can be determined by the ratio of these integrals (Figure S29):

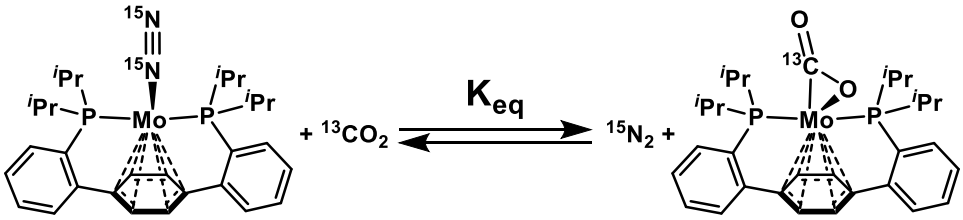

$$K_{eq} = \frac{[^{15}N_2][\mathbf{2}]}{[\mathbf{1}][^{13}CO_2]} = \frac{[^{15}N_2]}{[\mathbf{1}]}\frac{[\mathbf{2}]}{[^{13}CO_2]} = \frac{(0.37)}{(0.94)}\frac{(1.00)}{(0.87)} = 0.45$$

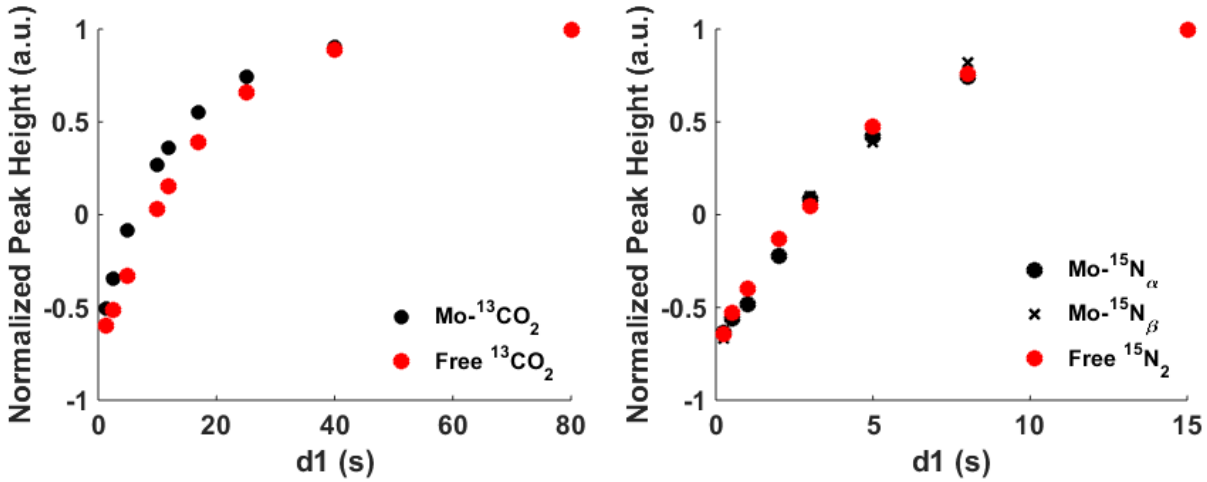

Figure S28—Peak intensities from ^{13}C (left) and ^{15}N (right) NMR inversion recovery experiments for an equilibrium mixture of **1-^{15}N** and **2-^{13}C**. The peak intensities for the free small molecule resonances are shown.

Table S3—Inversion Recovery Experiments for and Equilibrium Mixture of **1-^{15}N/2-^{13}C**.

	Mo-$^{13}CO_2$	**Free $^{13}CO_2$**	**Mo-$^{15}N_\alpha$**	**Mo-$^{15}N_\beta$**	**Free $^{15}N_2$**
T_1	12.5(4)	16.8(7)	5.2(4)	4.9(3)	4.9(3)
Average	--	--	5.1(4)		--

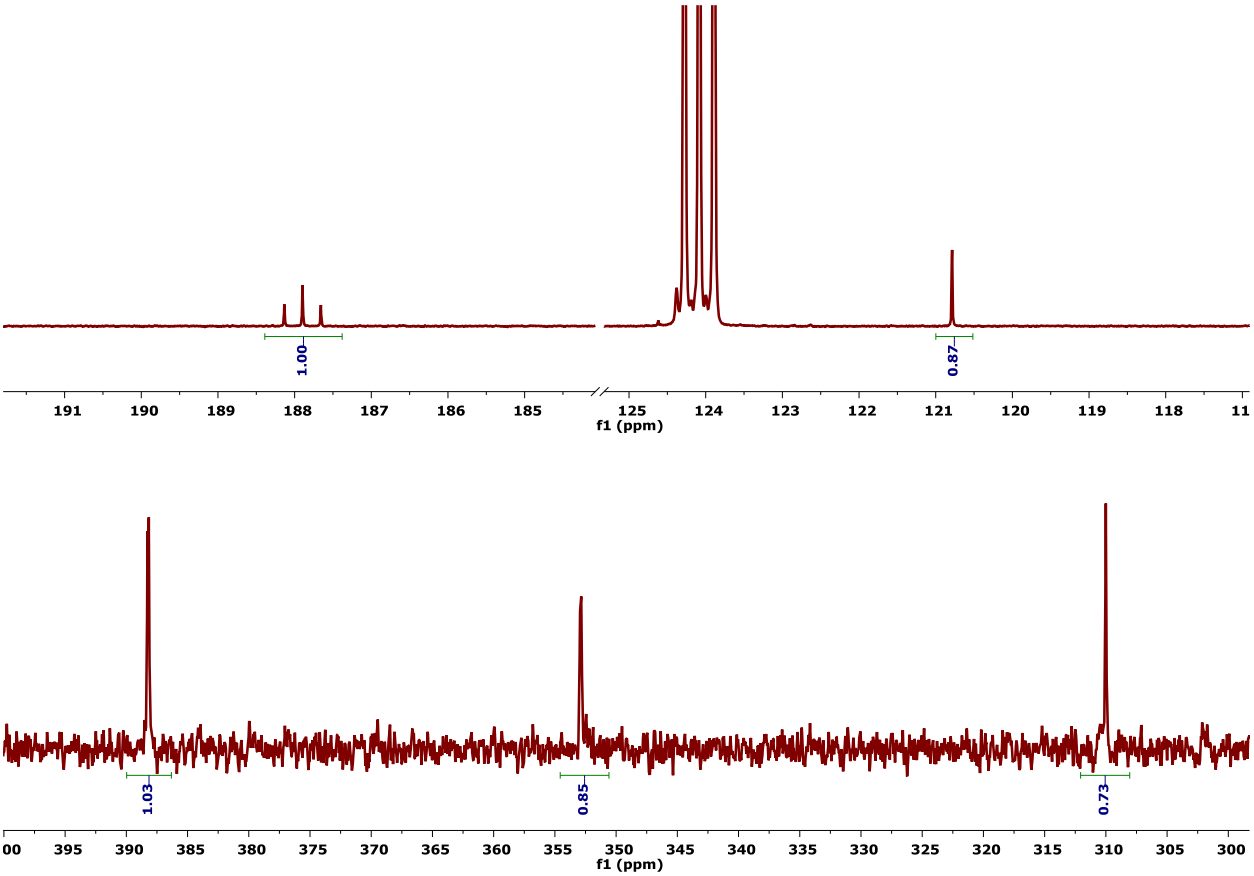

Figure S29—$^{13}C\{^{1}H\}$ (126 MHz, C_6D_6, 25 °C, d1 = 100 s) and $^{15}N\{^{1}H\}$ (51 MHz, C_6D_6, 25 °C, d1 = 25 s) NMR spectra of an equilibrium mixture of **1-^{15}N** and **2-^{13}C**.

To verify that the short and near-average T_1 times observed above were a manifestation of chemical exchange, a magnetization transfer experiment was conducted. Using the PRESAT pulse sequence in VnmrJ, a saturation pulse centered at free CO_2 (124.76 ppm) with a power of 4 dB was applied for 100 s. A second spectrum was collected with an off residence saturation pulse (100.0 ppm), as a control. The intensity of the bound $^{13}CO_2$ resonance is dampened in the former case, corroborating chemical exchange (Figure S30).

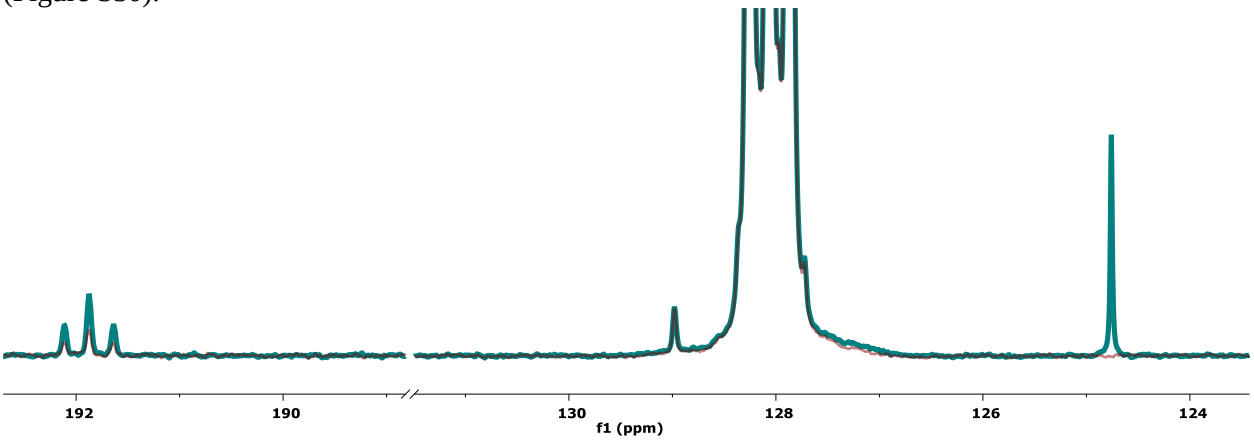

Figure S30—PRESAT $^{13}C\{^{1}H\}$ NMR spectrum (126 MHz, C_6D_6, 25 °C) demonstrating saturation transfer from free CO_2 (124.8 ppm) to bound CO_2 (191.9 ppm).

CO_2 Exchange Kinetics

General Procedure for Isotope Exchange Kinetics

In a N_2 filled glovebox, a J. Young NMR tube was charged with **2-^{13}C** (20 mg, 0.033 mmol), 1,3,5-trimethoxybenzene (10 mg, 0.059 mmol), and LA (0.033 mmol). The tube was sealed and attached to a high vacuum line. Following thorough evacuation of the headspace, the J. Young tube was backfilled with Ar gas. Under a heavy Ar counterflow, solvent (0.5 mL) was added via syringe. The tube was sealed and the contents mixed, affording a deep red homogeneous solution. $^{13}C\{^1H\}$ and $^{31}P\{^1H\}$ NMR spectra were collected at this point to confirm sample integrity and act as a T_0 reference point. The tube was attached to the vacuum line below a 33.4 mL calibrated volume and the contents frozen via submersion in LN_2. Following evacuation of the headspace, $^{12}CO_2$ (14.5 cm Hg in 33.4 mL, 0.265 mmol) was condensed into the tube. The tube contents were thawed, shaken once, and immediately introduced to an NMR probe pre-cooled to 0 °C for kinetic analysis.

Following collection of an array of $^{13}C\{^1H\}$ NMR spectra, a polynomial baseline correction and automatic phase correction was applied to all data. Max peak vs. time data was extracted for the isotopically enriched ^{13}C resonance corresponding to the Mo-$^{13}CO_2$ complexes. These data were normalized to the 1,3,5-trimethoxybenzene resonance at 93.0 ppm.

All data were fit, using the cftool feature of MatLab, according to a three-parameter exponential function:

$$y = a \times e^{(-b \times x)} + c$$

and the rate of exchange was determined according to the following equation:[10]

$$rate = \frac{[\boldsymbol{Mo}] \times [\boldsymbol{CO_2}] \times b}{[\boldsymbol{Mo}] + [\boldsymbol{CO_2}]}$$

The fraction of soluble $^{12/13}CO_2$ in each sample was estimated assuming rapid diffusion on the exchange timescale, equivalent solubility for $^{12}CO_2$ and $^{13}CO_2$, and approximating that all $^{13}CO_2$ originated from **2-^{13}C**. Under these conditions, the percent soluble CO_2 could be determined for each time point (t) as follows:

$$frac\ sol.CO_2 = \frac{1}{\frac{([Mo]_0 - [Mo]_t)}{[CO_2]_t}}$$

Averaging these values across all timepoints for a given sample, and across all samples, afforded average CO_2 solubilities of approximately 40% at the given temperature (0 °C) and pressure (*ca.* 2.4 atm).

Table S4—CO_2 Exchange Rate as a Function of LA Identity

	2 PhCl : Et_2O				
	Cs (BAr^F_{24})	**Na (BAr^F_{24})**	**Na (BAr^F_{24})‡**	**$B(C_6H_2F_3)_3$**	**$B(C_6F_5)_3$**
a	0.85	0.90	0.88	0.91	0.98
b	0.00088	0.00024	0.000067	0.00021	0.00036
c	0.12	0.10	0.10	0.10	0.13
R^2	0.99	0.99	0.99	0.99	0.99
rate	2 x 10^{-5}	6 x 10^{-6}	2 x 10^{-6}	5 x 10^{-6}	9 x 10^{-6}
	PhCl				
	NONE	**NONE†**	**$B(C_6H_2F_3)_3$**	**$B(C_6F_5)_3$**	**$B(C_6H_3(CF_3)_2)_3$**
a	0.90	0.85	0.87	0.88	0.75
b	0.011	0.0041	0.000058	0.000094	0.000040
c	0.10	0.10	0.12	0.10	0.15
R^2			0.99	0.99	0.97
rate	>2 x 10^{-4}	>7 x 10^{-5}	2 x 10^{-6}	2 x 10^{-6}	1 x 10^{-6}

‡The [Na(BAr^F_{24})] was doubled. †Run at -13 °C instead of 0 °C.

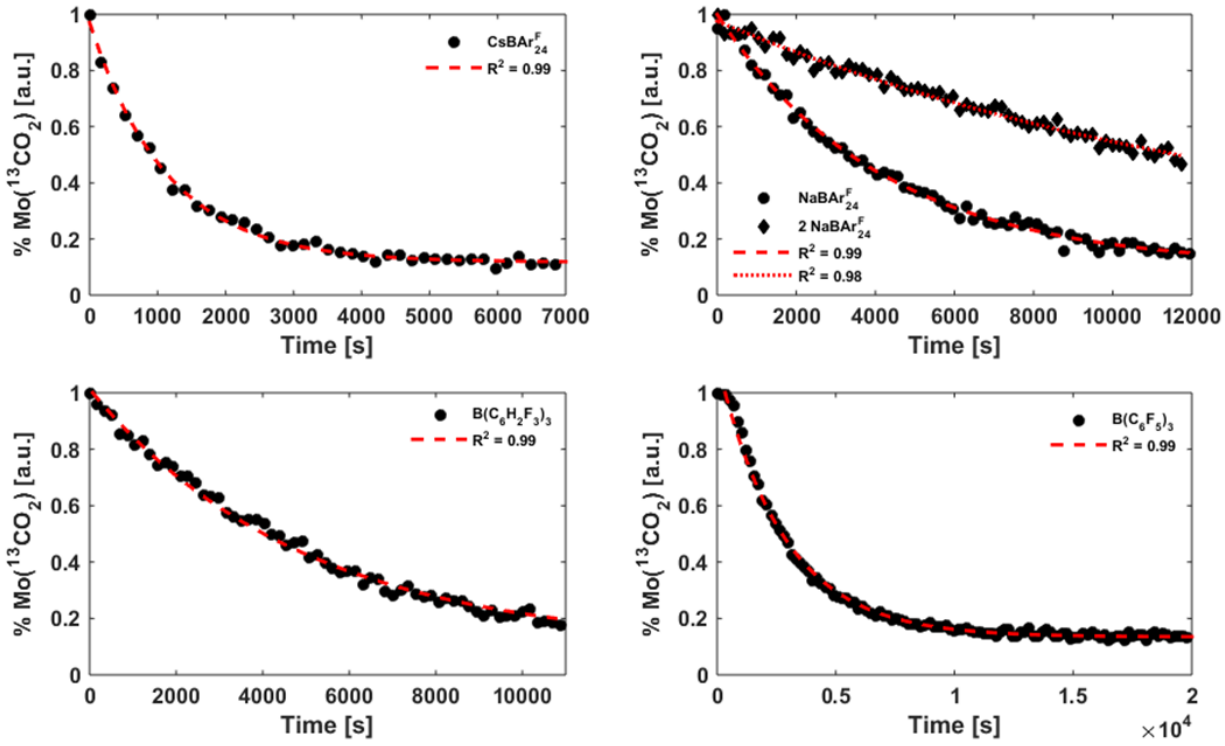

Figure S31—Representative $^{12/13}CO_2$ exchange data in 2 PhCl : Et_2O at 0 °C.

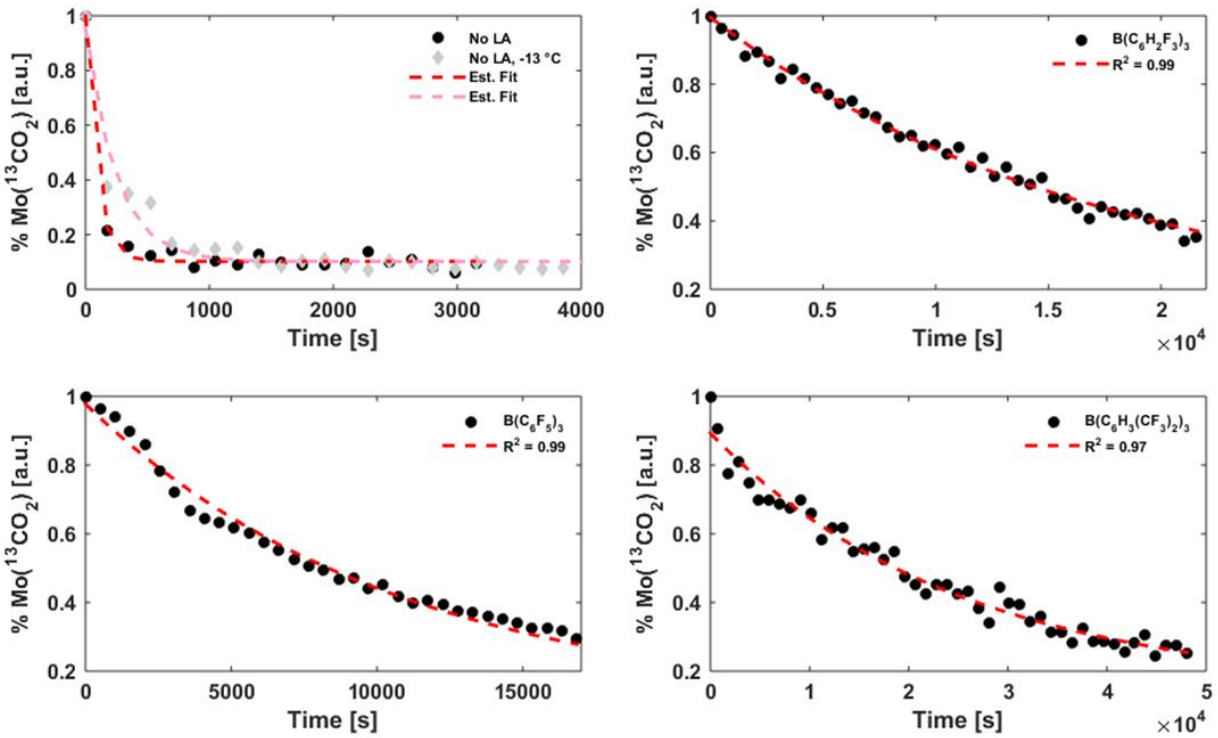

Figure S32—Representative $^{12/13}CO_2$ exchange data in PhCl at 0 °C (or -13 °C, gray).

The exponential rate data can be linearized as follows,

$$Ln(y - c) = -b \times X + Ln(a)$$

plotted, and fit with a linear regression to afford data that is qualitatively identical to the exponential fits.

Table S5—Linearized CO_2 Exchange Rate as a Function of LA Identity

	2 PhCl : Et_2O				
	Cs ($BAr^F{}_{24}$)	**Na ($BAr^F{}_{24}$)**	**Na ($BAr^F{}_{24}$)‡**	**$B(C_6H_2F_3)_3$**	**$B(C_6F_5)_3$**
b	0.00086	0.00027	0.000073	0.00016	0.00041
Ln(a)	-0.057	0.022	-0.025	0.0081	0.19
R^2	0.98	0.99	0.98	0.99	0.99
rate	2 x 10^{-5}	7 x 10^{-6}	2 x 10^{-6}	4 x 10^{-6}	10 x 10^{-6}
	PhCl				
	NONE	**NONE†**	**$B(C_6H_2F_3)_3$**	**$B(C_6F_5)_3$**	**$B(C_6H_3(CF_3)_2)_3$**
b	--	--	0.000064	0.00010	0.000041
Ln(a)	--	--	0.020	-0.057	-0.13
R^2	--	--	0.99	0.99	0.96
rate	--	--	2 x 10^{-6}	3 x 10^{-6}	1 x 10^{-6}

‡The [Na($BAr^F{}_{24}$)] was doubled. †Run at -13 °C instead of 0 °C.

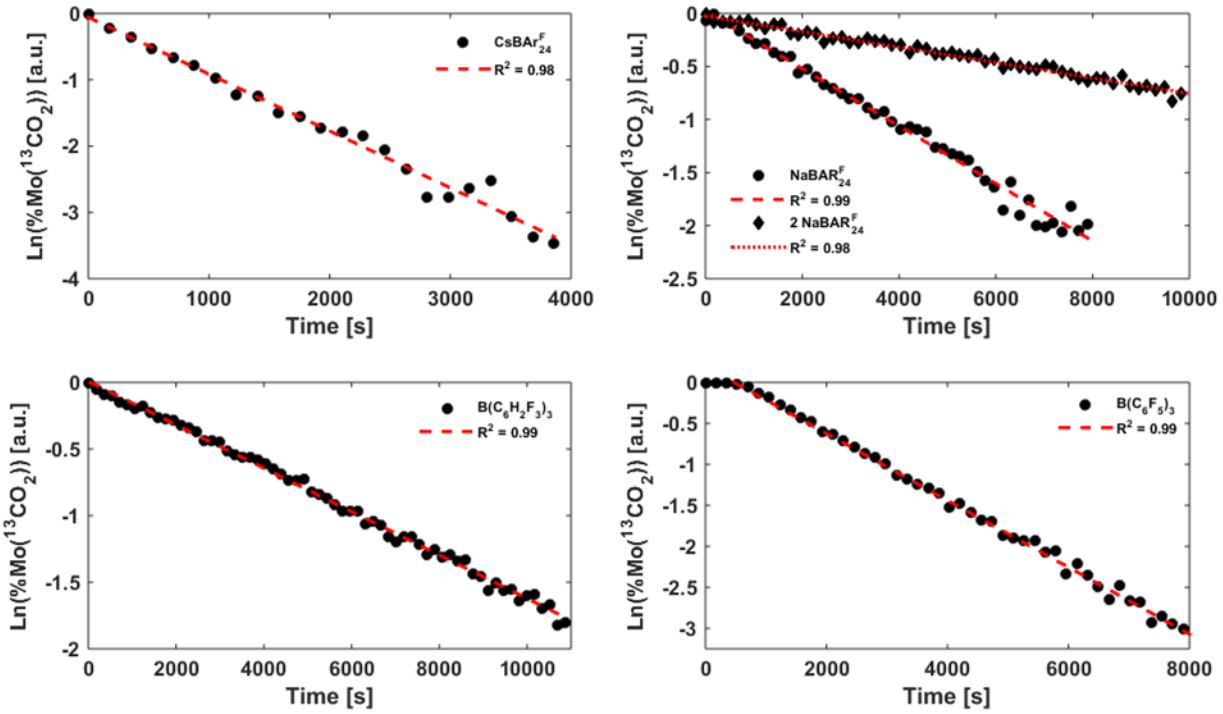

Figure S33—Linearized $^{12/13}CO_2$ exchange data in 2 PhCl : Et_2O at 0 °C.

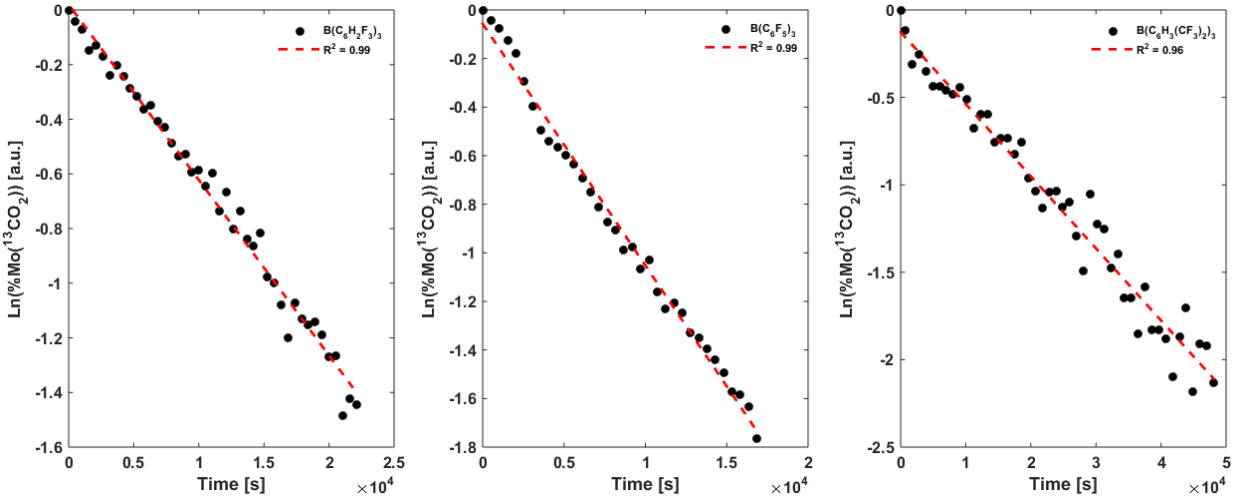

Figure S34—Linearized $^{12/13}CO_2$ exchange data in PhCl at 0 °C.

CO_2 Protonation Reactions

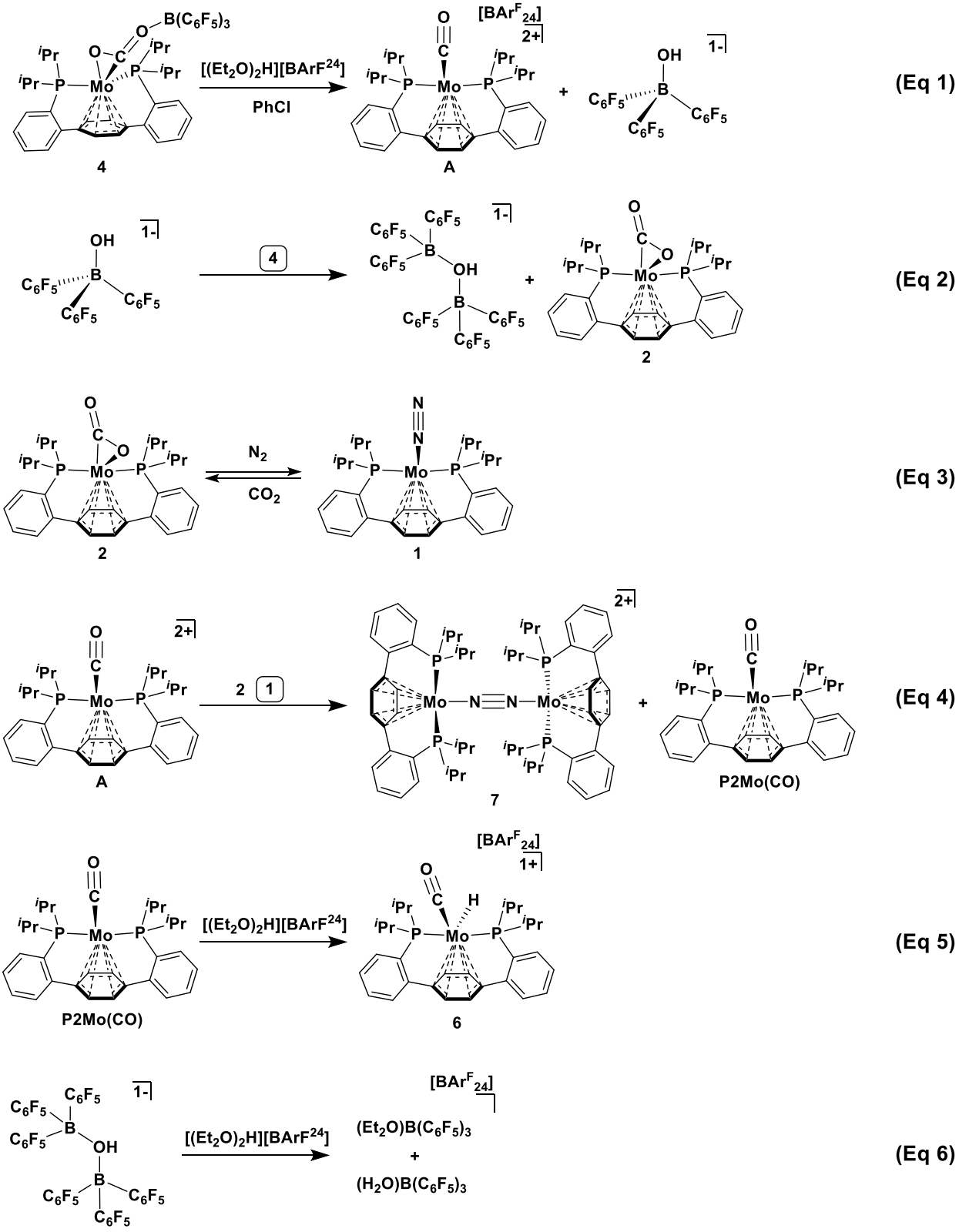

Scheme S1—Proposed mechanism for proton-induced CO_2 cleavage from **4**.

Under N_2:
In a typical reaction, a 20 mL scintillation vial was charged with **4-^{13}C** (40 mg, 0.036 mmol) and a stir bar. PhCl (1.5 mL) was added, providing a deep red solution. In a second vial, $[(Et_2O)_2H][BAr^F{}_{24}]$ (36 mg, 0.036 mmol) was dissolved in PhCl (1.5 mL), affording a colorless solution. With stirring, the acid solution was added to the solution of **4-^{13}C**, dropwise, resulting in a color change to yellow/green. $^{31}P\{^1H\}$, $^{13}C\{^1H\}$, and ^{19}F NMR spectroscopy evidence formation of **6-^{13}C**, $B(C_6F_5)_3$•Et_2O, $B(C_6F_5)_3$•H_2O, and a small amount of $[(B(C_6F_5)_3)_2OH]^-$ (Figure S36). Upon standing for 12 h, green X-ray quality crystals form, the identity of which was confirmed as **7**.

Reactions run analogously, but with 2 equiv. of $[(Et_2O)_2H][BAr^F{}_{24}]$ showed no remaining $[(B(C_6F_5)_3)_2OH]^-$ by ^{19}F NMR spectroscopy. Based on the borane speciation (confirmed by comparison to independently synthesized authentic samples) and the Mo complexes formed in the course of the reaction (deduced from independent reactivity, spectroscopy, and XRD), a plausible mechanism for the cleavage of CO_2 to CO and H_2O is outlined in Scheme S1. Such a mechanism accounts for the overall conversion to **6**—33% (^{31}P NMR spectroscopy)—observed experimentally.

Under Ar:
In a typical reaction, a 25 mL Teflon stoppered Schlenk tube was charged with **2-^{13}C** (30 mg, 0.050 mmol), LA (0.050 mmol), and a stir bar. The reaction vessel was attached to a high vacuum line and the headspace replaced with Ar. With a heavy Ar counterflow, the Teflon stopper was exchanged for a rubber septum. Solvent (3 mL, PhCl or 2 PhCl : Et_2O, *vide supra*) was added via syringe and the stopper replaced. Stirring was initiated, affording a deep red homogeneous solution. The reaction was cooled to -78 °C with a dry ice/acetone slush bath, and with a heavy Ar counterflow, solid $[(Et_2O)_2H][BAr^F{}_{24}]$ was added. The flask was quickly sealed, removed from the line, and shaken. After warming to RT, volatiles were removed under reduced pressure, giving a dark residue. This residue was dissolved in a THF solution of PPh_3 (6 mg, 0.023 mmol in 1 mL). A 0.5 mL aliquot of the resulting solution was transferred to an NMR tube and analyzed by $^{31}P\{^1H\}$ and $^{13}C\{^1H\}$ NMR spectroscopy. The extent of C–O cleavage was determined by integration of the resonance for **6-^{13}CO** (^{31}P δ = 93.01 ppm) against a protonated O=PPh_3 standard (O=PPh_3 is protonated by the excess acid present in the reaction mixture).

Table S6—C–O Bond Cleavage as a Function of LA Additive

	LA Additive	Absolute % C–O Cleavage[b]	Relative % C–O Cleavage[c]	Material Balance[d]
2 PhCl : Et_2O	**NONE**	0	0	--
	$Cs(BAr^F{}_{24})$	7	21	80 %
	$Na(BAr^F{}_{24})$	4	12	103 %
	$Na(BAr^F{}_{24})$[a]	5	15	104 %
	$B(C_6H_2F_3)_3$	4	12	98 %
	$B(C_6F_5)_3$	9	27	89 %
PhCl	**NONE**	3	9	92 %
	NONE[e]	10	30	--
	$B(C_6H_2F_3)_3$	13	39	88 %
	$B(C_6F_5)_3$	17	51	96 %
	$B(C_6H_3(CF_3)_2)_3$	16	48	109 %

[a]The $[Na(BAr^F{}_{24})]$ was doubled. [b]Average of two runs. [c]Normalized to a theoretical maximum of 33% cleavage. [d]Sum of known diamagnetic Mo species in the final reaction mixture (2 equiv. of Mo are assumed to make dinuclear **7** for each equiv. of **6-^{13}CO** formed). [e]Run in thawing PhCl.

Table S7—Comparison of CO_2 Activation, Kinetic Stabilization, and Protonation Data

	LA Additive	AN	δ $^{13}CO_2$ (ppm)	Rate x 10^{-6} (s^{-1})	Residence Time† x 10^6 (s)	% C–O Cleavage	
						Abs.	Rel.
2 PhCl : Et_2O	NONE	12.4	192.3	>200	0.005	0	0
	$Cs(BAr^F{}_{24})$	23.7	199.9	20	0.05	7	21
	$Na(BAr^F{}_{24})$	31.8	203.5	6	0.2	4	12
	$B(C_6H_2F_3)_3$	68.1	215.3	5	0.2	4	12
	$B(C_6F_5)_3$	79.2	219.3	9	0.1	9	27
PhCl	NONE	13.2	192.9	>200	0.005	3	9
	$B(C_6H_2F_3)_3$	67.9	215.7	2	0.5	13	39
	$B(C_6F_5)_3$	78.1	219.6	2	0.5	17	51
	$B(C_6H_3(CF_3)_2)_3$	82.7	219.1	1	1.0	16	48

†The "residence time" of the bound CO_2 unit was determined by taking the inverse of the self-exchange rate.

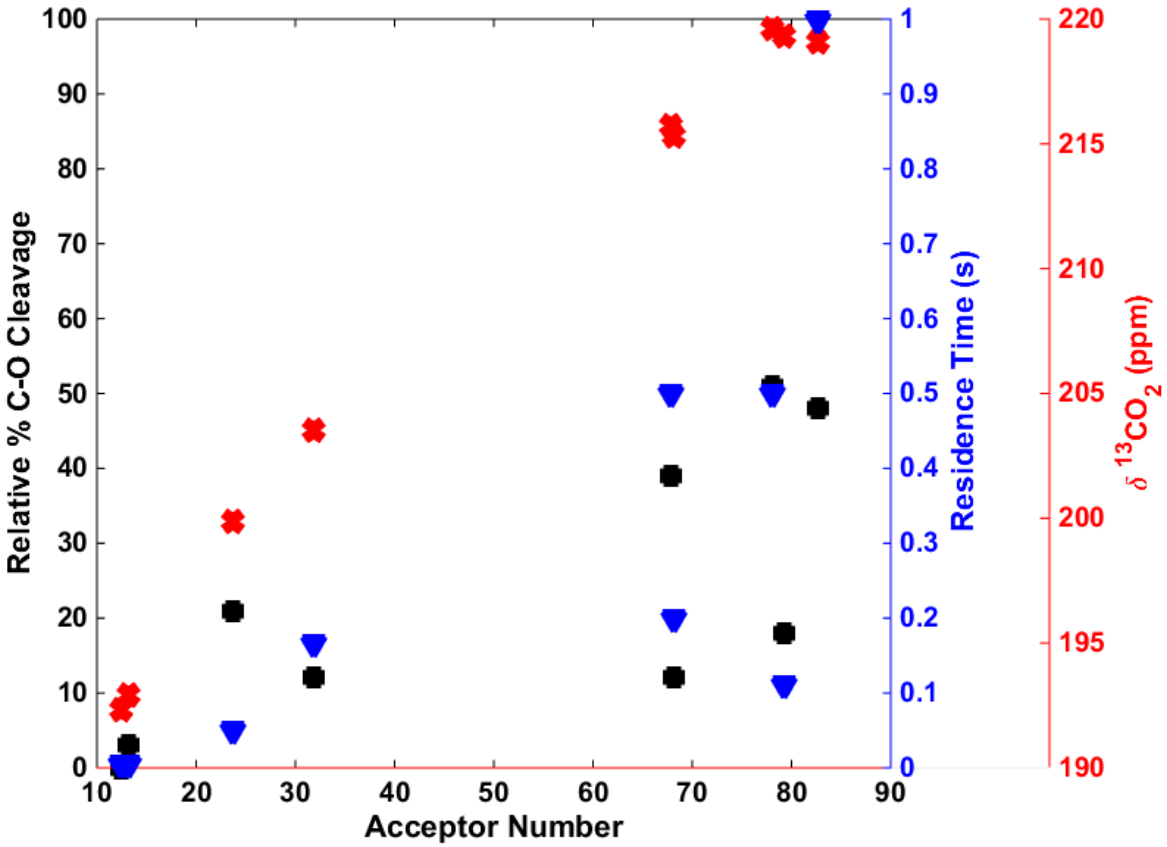

Figure S35—Graphical comparison of the degree of C–O bond cleavage (■), CO_2 adduct kinetic stabilization (▼), and thermodynamic C–O bond activation (**X**) for **2-$^{13}CO_2$** and LA adducts thereof.

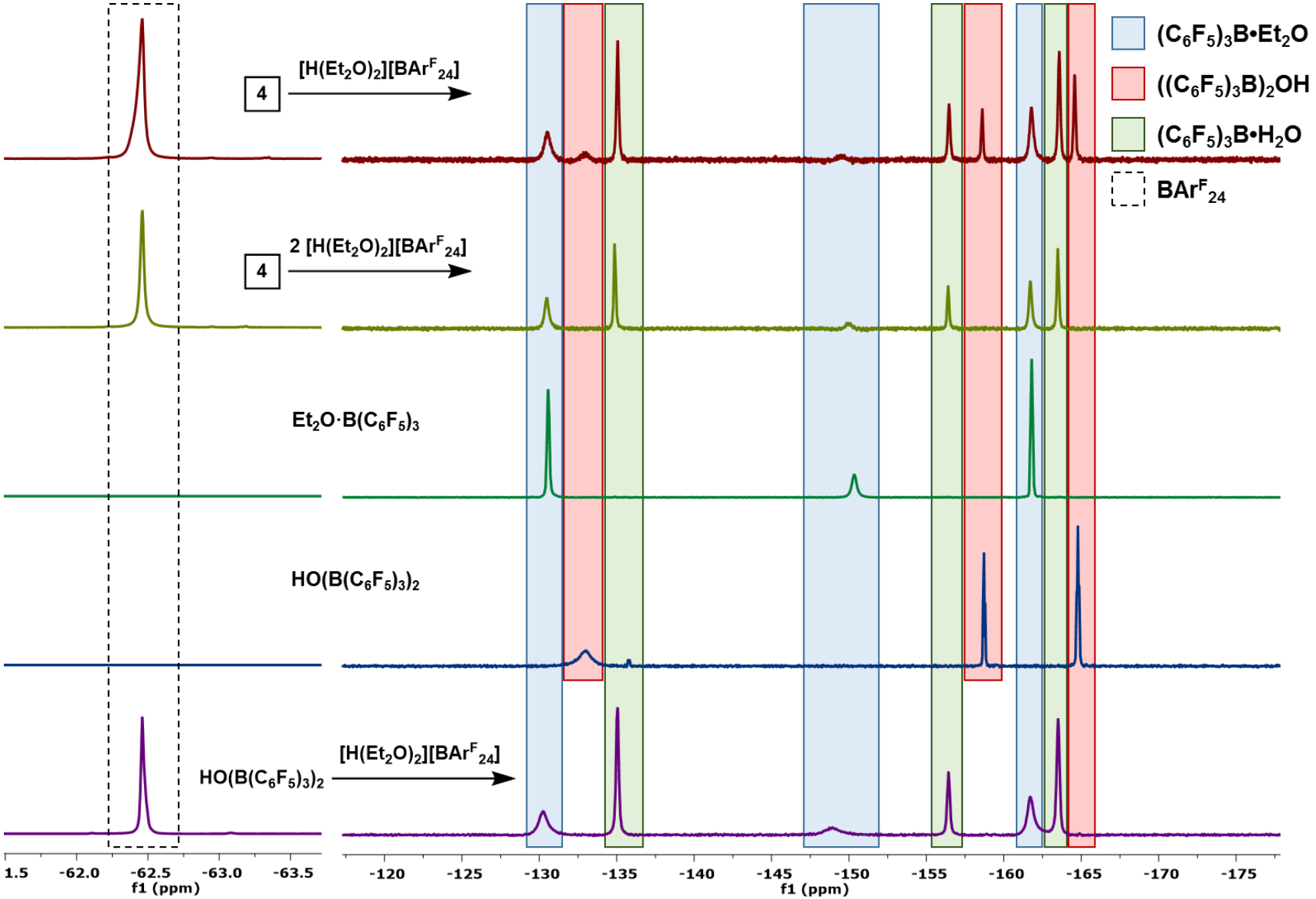

Figure S36— $B(C_6F_5)_3$ speciation following CO_2 protonation reactions as reported by ^{19}F NMR spectroscopy (376 MHz, PhCl, 23 °C). Spectra of authentic samples are provided for reference.

Crystallographic Information

CCDC deposition numbers 1859319-1859323 contain the supplementary crystallographic data for this paper. These data can be obtained free of charge from The Cambridge Crystallographic Data Centre via www.ccdc.cam.ac.uk/data_request/cif.

Refinement Details

In each case, crystals were mounted on a MiTeGen loop using Paratone oil, then placed on the diffractometer under a nitrogen stream. Low temperature (100 K) X-ray data were obtained on a Bruker D8 VENTURE Kappa Duo PHOTON 100 CMOS based diffractometer (Mo $I_{\mu}S$ HB micro-focus sealed X-ray tube, K_{α} = 0.71073 Å). All diffractometer manipulations, including data collection, integration, and scaling were carried out using the Bruker APEXIII software.[11] Absorption corrections were applied using SADABS.[12] Space groups were determined on the basis of systematic absences and intensity statistics and the structures were solved in the Olex 2 software interface[13] by intrinsic phasing using XT (incorporated into SHELXTL)[14] and refined by full-matrix least squares on F^2. All non-hydrogen atoms were refined using anisotropic displacement parameters. Hydrogen atoms were placed in the idealized positions and refined using a riding model, unless noted otherwise. The structures were refined (weighed least squares refinement on F^2) to convergence. Graphical representations of structures with 50% probability thermal ellipsoids were generated using the Diamond 3 visualization software.[15]

Table S8—Crystal and refinement data for complexes **2 - 4**, **6**, & **7**.

	2	**3**	**4**	**6**	**7**
CCDC Number[16]	1859319	1859320	1859321	1859322	1859323
Empirical formula	$C_{37}H_{46}MoO_2P_2$	$C_{48}H_{40}BF_{15}MoN_2P_2$	$C_{49}H_{40}BF_{15}MoO_2P_2$	$C_{75}H_{64}BF_{24}MoOP_2$	$C_{130}H_{109}B_2ClF_{48}Mo_2N_2P_4$
Formula weight	680.62	1098.51	1114.50	1605.95	2984.02
T (K)	100	100	100	100	100
a, Å	8.773(3)	23.5019(11)	9.4051(4)	13.0216(7)	13.0558(8)
b, Å	11.504(3)	9.3504(5)	11.3058(5)	16.2787(8)	16.4548(10)
c, Å	16.681(5)	20.5286(9)	22.0674(10)	18.3832(9)	16.5050(10)
α, °	93.575(10)	90	103.065(2)	111.964(2)	65.959(2)
β, °	98.963(9)	90	94.669(2)	100.228(3)	81.517(2)
γ, °	103.528(10)	90	96.976(2)	92.383(3)	78.563(2)
Volume, Å^3	1608.3(8)	4511.2(4)	2254.39(17)	3531.5(3)	3165.1(3)
Z	2	4	2	2	1
Crystal system	Triclinic	Orthorhombic	Triclinic	Triclinic	Triclinic
Space group	$P\bar{1}$	$Pca2_1$	$P\bar{1}$	$P\bar{1}$	$P\bar{1}$
d_{calc}, g/cm^3	1.405	1.617	1.642	1.510	1.566
θ range, °	1.830 to 28.726	1.984 to 31.511	0.953 to 36.319	1.358 to 33.250	2.410 to 39.996
μ, mm^{-1}	0.540	0.462	0.466	0.340	0.392
Abs. Correction	Semi-empirical	Semi-empirical	Semi-empirical	Semi-empirical	Semi-empirical
GOF	1.044	1.008	0.988	1.242	1.030
R_1 ,[a] wR_2 [b] [I>2 σ(I)]	0.0719, 0.1592	0.0371, 0.0668	0.0268, 0.0647	0.0430, 0.0977	0.0557, 0.1344
Radiation Type	Mo K_α	Mo K_α	Mo K_α	Mo K_α	Mo K_α

[a] $R_1 = \sum||F_o| - |F_c||/\sum|F_o|$. [b] $wR_2 = [\sum[w(F_o^2-F_c^2)^2]/\sum[w(F_o^2)^2]^{1/2}$.

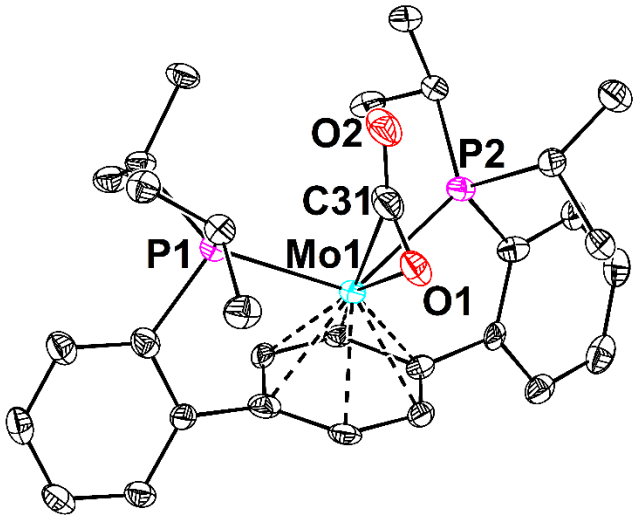

Figure S37—Structural drawing of **2** with 50% probability anisotropic displacement ellipsoids. H-atoms are omitted for clarity.

Special Refinement Details: The CO_2 ligand (C31, O1, and O2) in **2** was positionally disordered but satisfactorily modeled over two positions. To prevent the minor component (40%) from refining as non-positive definite, similarity restraints on Uij and rigid bond restraints were applied to the disordered unit.

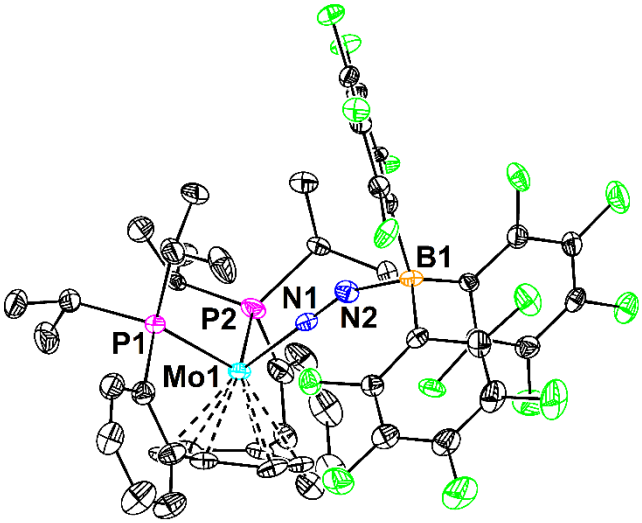

Figure S38—Structural drawing of **3** with 50% probability anisotropic displacement ellipsoids. H-atoms are omitted for clarity.

Special Refinement Details: The $B(C6F5)_3$ motif in **3** was positionally disordered but satisfactorily modeled over two positions. Similarity restraints on U_{ij} and rigid bond restraints were applied to the entire perfluoroaryl borane (B1 and C31 through F15).

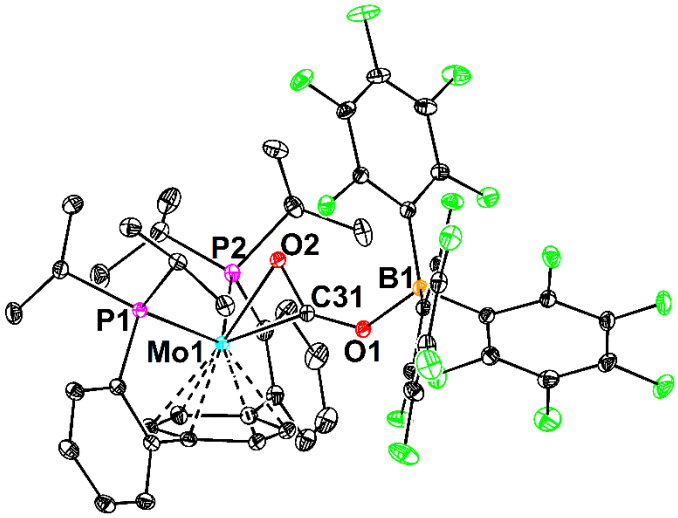

Figure S39—Structural drawing of **4** with 50% probability anisotropic displacement ellipsoids. H-atoms are omitted for clarity.

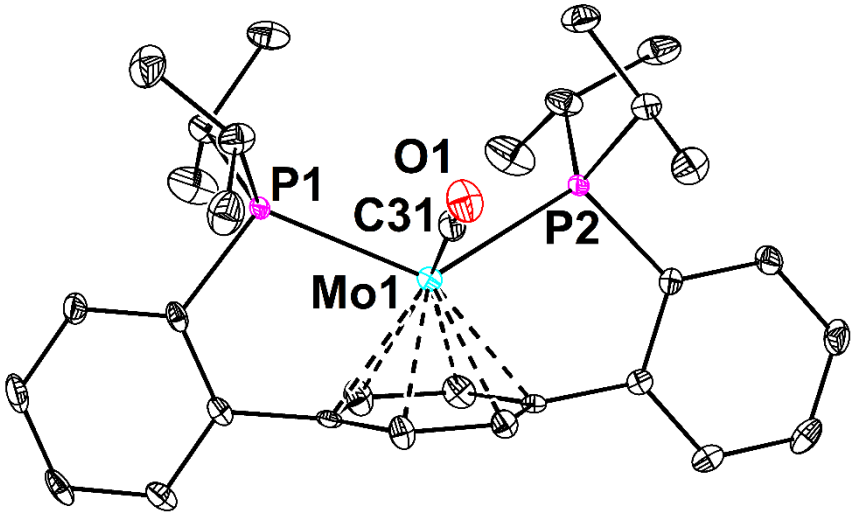

Figure S40—Structural drawing of **6** with 50% probability anisotropic displacement ellipsoids. H-atoms and the BAr^{F}_{24} counterion are omitted for clarity.

Special Refinement Details: The solid-state structure of **6** demonstrated whole molecule disorder in two independently grown crystals. This was not a temperature dependent phenomenon and collecting data at higher temperature did not resolve the disorder.

The disordered *para*-terphenyl diphosphine Mo fragments (Mo1 through C31) were modeled satisfactorily over two positions in a relative population of 85 : 15. Due to the close overlap of these moieties, refinements with an anisotropic minor component were not stable. We elected to leave the minor component isotropic in the final refinement cycles, applying enhanced rigid bond restraints. Along with the whole molecule disorder of the main residue, three of the CF_3 groups of the counterion displayed rotational disorder. These positional disorders were well modeled over two discreet positions and refined with enhanced rigid bond restraints.

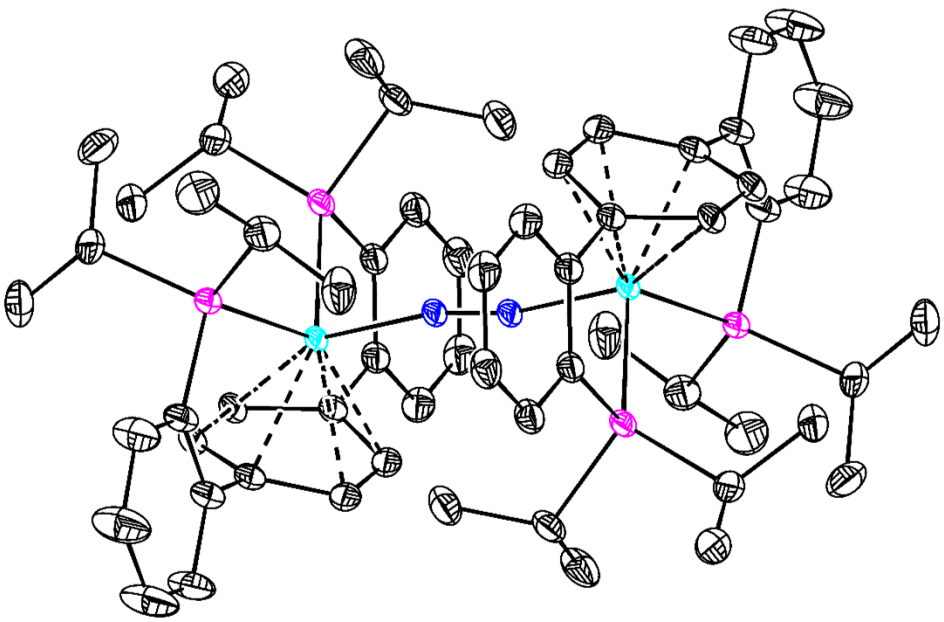

Figure S41—Structural drawing of **7** with 50% probability anisotropic displacement ellipsoids. H-atoms and two BAr^{F}_{24} counterions are omitted for clarity.

Special Refinement Details: The BAr^{F}_{24} counterion displayed significant positional disordered of both the CF3 groups and one of the aryl rings. These disorders were satisfactorily modeled over two (or three) discreet positions. The entire counterion was refined with enhanced rigid bond restraints applied. Additionally, significant unassigned electron density was observed in the Fourier difference map 0.83 Å from Mo1. This can be attributed to the Mo center of a minor (2.7%) disordered component. Due to the low population of this second component, the lighter atoms were not discernable and the disorder could not be well modeled.

References

(1) Pangborn, A. B.; Giardello, M. A.; Grubbs, R. H.; Rosen, R. K.; Timmers, F. J. *Organometallics* **1996**, *15*, 1518.
(2) Buss, J. A.; Edouard, G. A.; Cheng, C.; Shi, J.; Agapie, T. *J. Am. Chem. Soc.* **2014**, *136*, 11272.
(3) Mon, I.; Jose, D. A.; Vidal-Ferran, A. *Chem. Eur. J.* **2013**, *19*, 2720.
(4) Lesley, M. J. G.; Norman, N. C.; Rice, C. R.; Reger, D. L.; Little, C. A.; Lamba, J. J. S.; Brown, K. J.; Peters, J. C.; Thomas, J. C.; Sahasrabudhe, S.; Yearwood, B. C.; Atwood, D. A.; Hill, R. F.; Wood, G. L.; Danzer, R.; Paine, R. T.; Wagner, N. L.; Murphy, K. L.; Haworth, D. T.; Bennett, D. W.; Byers, P. K.; Canty, A. J.; Honeyman, R. T.; Arnáiz, F. J.; Miranda, M. J.; Bohle, D. S.; Sagan, E. S.; Chivers, T.; Sandblom, N.; Schatte, G. In *Inorg. Synth.*; Vol. 34; Wiley: Hoboken, NJ 2004.
(5) Nicasio, J. A.; Steinberg, S.; Inés, B.; Alcarazo, M. *Chem. Eur. J.* **2013**, *19*, 11016.
(6) Soltani, Y.; Wilkins, L. C.; Melen, R. L. *Angew. Chem. Int. Ed.* **2017**, *56*, 11995.
(7) Herrington, T. J.; Thom, A. J. W.; White, A. J. P.; Ashley, A. E. *Dalton Trans.* **2012**, *41*, 9019.
(8) Brookhart, M.; Grant, B.; Volpe, A. F. *Organometallics* **1992**, *11*, 3920.
(9) Fulmer, G. R.; Miller, A. J. M.; Sherden, N. H.; Gottlieb, H. E.; Nudelman, A.; Stoltz, B. M.; Bercaw, J. E.; Goldberg, K. I. *Organometallics* **2010**, *29*, 2176.
(10) Moore, J. W.; Pearson, R. G. *Kinetics and Mechanism*; 3rd ed.; Wiley: New York, NY 1981.
(11) APEX3, Version 1 User Manual, M86-EXX229, Bruker Analytical X-ray Systems, Madison, WI, May 2016.
(12) Sheldrick, G.M. "SADABS (version 2008/1): Program for Absorption Correction for Data from Area Detector Frames", University of Göttingen, 2008.
(13) Dolomanov, O. V.; Bourhis, L. J.; Gildea, R. J.; Howard, J. A. K.; Puschmann, H. *J. Appl. Crystallogr.* **2009**, *42*, 339.
(14) Sheldrick, G.M. *Acta. Cryst.*, **2008**, *A64*, 112.
(15) Brandenburg, K. (1999). DIAMOND. Crystal Impact GbR, Bonn, Germany.
(16) Crystallographic data have been deposited at the CCDC, 12 Union Road, Cambridge CB2 1EZ, UK and copies can be otained on request, free of charge, by quoting the publication citation and the respective deposition numbers.